NTNU
Norwegian University of
Science and Technology

# Quantum Monte Carlo Simulations of Drag Interaction in the Superfluid Phase of the 3-Component Bose-Hubbard Model

Eirik Erlandsen

Master of Science in Physics and Mathematics
Submission date: June 2018
Supervisor: Asle Sudbø, IFY

Norwegian University of Science and Technology
Department of Physics

# Preface

This thesis presents research conducted during the spring semester of the final year of the five-year Master's Degree Program in Applied Physics and Mathematics at the Norwegian University of Science and Technology (NTNU). Parts of the material related to cold atom systems is based on my specialization project *Ultracold Spin-Orbit Coupled Spinor-One Bosons on a Square Optical Lattice in the Strong Coupling Regime*, which was completed during the preceding semester. I would like to thank my supervisor Prof. Asle Sudbø for excellent guidance and my friends at the Department of Physics at NTNU, UC Berkeley and the University of Chicago for fruitful discussions. I would especially like to thank Stian Hartman, Master's student at the department of physics at NTNU, whom I collaborated with during the final part of the semester. This collaboration resulted in a paper which is awaiting approval and has been posted to arXiv [1]. The research presented in this thesis was supported in part with computational resources at NTNU provided by NOTUR, and built on code provided by the ALPS project[2–4] and Even Thingstad, PhD student at the Department of Physics at NTNU.

Eirik Erlandsen
Trondheim, Norway
June, 2018

# Abstract

We study Andreev-Bashkin drag interactions between the superflow of different components in the superfluid phase of a three-component Bose-Hubbard model without component-mixing interactions, relevant for cold atom systems subjected to an optical lattice. By means of directed worm algorithm path integral Monte Carlo simulations we produce the phase diagram of the superfluid drag density as a function of the nearest-neighbor hopping amplitude and the chemical potential in the case of component-symmetric parameters. In both one and two dimensions, we find an expected region of negative drag close to the tip of the first Mott lobe and a generalization of the two-component supercounterfluid phase in parts of this region. In addition, we also find a more trivial positive drag with strongest presence below the Mott lobe. Further, we investigate the dependence of the drag on the details of the intercomponent interactions strengths in the weakly-coupled regime. In accordance with mean-field results obtained by Stian Hartman, we find that, unlike in the two-component case, the drag is no longer independent of the sign of the intercomponent interaction strengths. In particular, the drag between component $a$ and $b$ can either be strengthened or weakened by increasing interaction strength between component $a$ and $c$, depending on the sign of the interaction strength between $b$ and $c$.

# Sammendrag

Vi studerer Andreev-Bashkin drag-interaksjoner mellom ulike superfluide komponenter i den superfluide fasen til en tre-komponent Bose-Hubbard modell med komponent-konserverende interaksjoner. Denne modellen er relevant for kalde atomsystemer på et optisk gitter. Ved hjelp av orm-algoritme vei-integral Monte Carlo simuleringer fremstiller vi fasediagrammet for superfluid drag som funksjon av nærmeste-nabo-hoppe-amplitude og kjemisk potensial for komponent-symmetriske parametere. I både én og to dimensjoner finner vi en forventet fase med negativt drag i nærheten av tuppen av den første Mott-loben. I deler av dette området observerer vi også en super-motstrøm-fase. Utenfor det negative området finner vi et mer trivielt, positivt drag som er tydeligst tilstede under Mott-loben. Videre undersøker vi avhengigheten til draget med hensyn på detaljene til interkomponent-interaksjonsstyrkene i det svakt koblede regimet. I samsvar med middelfelt-resultater fremskaffet av Stian Hartman, finner vi, i motsetning til to-komponent-tilfellet, at draget ikke lenger er uavhengig av fortegnet til interkomponent-interaksjonsstyrekene. Spesifikt viser vi at draget mellom komponent $a$ og $b$ kan bli enten styrket eller svekket av økt interaksjonsstyrke mellom komponent $a$ og $c$, avhengig av fortegnet til interaksjonen mellom $b$ og $c$.

# Contents

# Chapter 1

# Introduction

## 1.1 Background and Motivation

Following the experimental realization of the first gaseous Bose-Einstein condensate (BEC) in 1995 [5, 6], which was awarded the 2001 Nobel Prize in physics [7, 8], the area of cold atom systems has become a hot topic in physics [9]. Cold atom systems are simply systems consisting of atoms that are maintained at very low temperatures using advanced trapping and cooling techniques. They are attractive to work with due to their tunability and absence of impurities, which are not typical qualities of normal physical systems. Of special interest is the opportunity of subjecting a condensate to a spatially periodic potential that acts as a crystal lattice with tunable potential well depth and periodicity [10]. This allows for examination of analogues to condensed matter systems under more ideal and adjustable conditions, as well as exploration of parameter regimes that are normally inaccessible [11]. Due to these properties, in addition to their tendency of exhibiting quantum behavior, cold atomic systems are suitable candidates for quantum simulations [12].

It is also possible to have so-called multicomponent or multispecies condensates, which are condensates with an internal degree of freedom, leading to more than one macroscopically occupied quantum state [11]. The introduction of additional, interacting, components in the system introduces new dynamics and can lead to interesting phenomena. The different components can be completely different atoms, different isotopes of the same atom or atoms of the same type in different hyperfine states [13]. The last type can be used to explore the effects of strong spin-orbit coupling by coupling the motion of the particles to induced transitions between the different hyperfine states, producing the same type of interaction that is experienced by particles with a nonzero magnetic moment moving in an electric field [14]. The effects of spin-orbit coupling are of interest due to their relevance for topological insulators, spintronic devices and quantum computing [15].

A special case of a multicomponent condensate is when the components are different hyperfine states that constitute a complete hyperfine multiplet. A system of this type can form a spinor condensate [16], where the internal degree of freedom is an actual spin degree of freedom, described by a spherical tensor in spin space [13]. This changes the symmetry of the system and shapes the interaction term in the Hamiltonian [11], demanding, for instance, that spinor condensates have component-mixing interactions of the type where e.g. one particle with spin up and one particle with spin down scatter into two particles with spin zero, in the spinor-1 case. Such component-mixing interactions can be present, in general, in hyperfine mixtures and can significantly reduce the lifetime of the condensate if they produce hyperfine states that are not confined by the trapping potential [13]. In this thesis, we will focus on the case of a general three-component system were such non-component-conserving interactions can be neglected.

The first multicomponent condensate that was produced consisted of two hyperfine states of $Rb^{87}$ [17] and was obtained by accident when atoms in two hyperfine states, that turned out to have strongly suppressed component-mixing interactions, were introduced into the system [7]. Later, condensates with different combinations of two hyperfine states of $Rb^{87}$ have been realized [18, 19]. There has also been produced condensates consisting of atoms of both $Rb^{87}$ and $K^{41}$ [20, 21] as well as both $Rb^{85}$ and $Rb^{87}$ [22]. Spinor-1 condensates, consisting of three different components, have been obtained for $Na^{23}$ [23] and $Rb^{87}$ [24], while spinor-2 condensates have been realized for $Rb^{87}$ [25, 26]. On optical lattices, a mixture of $Rb^{87}$ and $K^{41}$ [27] has been produced, and the scattering lengths of spinor $Rb^{87}$ [28] as well as a variety of properties of two-component hyperfine mixtures [29–31], including superfluid properties [32], have been explored experimentally.

As we will discuss further in this thesis, the introduction of several interacting components in a superfluid produces a dissipationless drag between the different superfluid components, called the Andreev-Bashkin effect, which was first studied in the context of a mixture of superfluid $He^4$ and $He^3$ [33]. The drag impacts the flow of the different components and leads, for instance, to a moving component inducing a mass flow of a different component at rest. Due to the low miscibility of a mixture of $He^4$ and $He^3$, this system has proven to be a poor arena for exploration of such behavior [34]. The multicomponent superfluids that are needed to produce the effect are, however, realizable in cold atom systems [35–37]. According to [34] it could be possible to investigate drag effects in two-component systems using already existing experimental techniques by focusing on the relationship between the speed of sound and the magnetic susceptibility instead of trying to directly measure induction of mass currents.

In addition to superfluid systems, drag interactions are expected to be important for the physics of nuclear Fermi liquids in neutron stars [38, 39], consisting of a superfluid mixture of neutrons and Cooper paired protons, as well as multicomponent superconducting systems [40]. For superfluid systems, the significance of the drag effect is rooted in the fact that such systems depend strongly on the formation and interaction of quantum vortices [41, 42], which again are considerably influenced by drag interactions [43–46]. The introduction of multiple components leads to a wider range of possible vortices, including composite vortices which can be more energetically favorable than elementary vortices in the presence of the drag effect, producing a broader spectrum of topological phase transitions.

The dependence of the drag on microscopic parameters has been investigated numerically in the two-component case on an optical lattice through quantum Monte Carlo simulations [46–48]. The drag has been found to mostly take on positive values, meaning that superflow of component $a$ induces a superflow of component $b$ in the same direction, a so-called co-flow. However, in a certain region with filling factor close to 1, near the transition to a Mott-insulating phase, the drag has been found to take on negative values, meaning that a flow of component $a$ induces a flow of component $b$ in the opposite direction, a so-called counter-flow. For sufficiently strong intercomponent interactions and component-symmetric parameters, there have also been found phases where the magnitude of the superfluid drag density approaches the magnitude of the ordinary superfluid densities, named a *paired superfluid* phase or a *supercounterfluid* phase depending on whether there is co-flow or counter-flow between the components. In the supercounterfluid phase, the total superfluid density vanishes, while the normal superfluid densities and the superfluid drag density are nonzero respectively. In the two-component case, the microscopic origin of the drag has also been investigated analytically in the weakly-coupled limit in free space [49] and on an optical lattice using a mean-field approach [50, 51] and the plane-wave expansion method [52].

On this background we turn to the three-component case on an optical lattice, investigating the drag interactions using path integral Monte Carlo simulations. Of special interest is how the supercounterfluid phase is affected by the presence of an additional component, which is related to the fact that

there are now three different components in the system, but still only two opposite ways to move in a given direction. The third component will also generally impact the strength of the drag between the two other components in the case of positive drag, which will be investigated in some specific cases of interest in the weakly coupled regime.

## 1.2 Structure

The necessary background material for cold atom systems and superfluidity, as well as the theory related to the Monte Carlo simulations, is presented in chapter 2. We start by introducing the concept of Bose-Einstein condensation before we give a short introduction to cold atom systems and the theoretical description of multicomponent cold bosonic systems on an optical lattice through the Bose-Hubbard model. We then cover the basics of superfluidity, focusing on a classical field description to establish important concepts such as twisted boundary conditions, before we move on to the hydrodynamics of multicomponent superfluids. For the Monte Carlo part, we start with Monte Carlo integration from a purely mathematical perspective followed by applications of Monte Carlo integration in classical statistical mechanics, covering Markov chains and the Metropolis-Hastings algorithm in the process. We then connect the material related to classical statistical mechanics to the quantum system described by the Bose-Hubbard model by invoking the path integral formulation of the partition function. We explain how the resulting classical configurations contributing to the partition function can be understood in terms of periodic particle trajectories in imaginary time and how these particle trajectories relate to the superfluid densities of the system. We then give a throughout introduction to the worm algorithm, which is used to generate new configurations in the Monte Carlo simulations, before we comment briefly on the sign problem that complicate the simulation of e.g. fermionic systems. In chapter 3 we present the results of the simulations that have been performed in both the strongly and weakly coupled regimes, discuss these results and compare them to relevant sources in the literature. In chapter 4, we summarize the results and their implications for further work. Finally, the details of the numerics are presented in the appendix.

# Chapter 2

# Background Material

## 2.1 Conventions

Vectors will be denoted by arrows, e.g. the position vector $\vec{r}$. A sum over nearest neighbors on a lattice will be expressed as

$$\sum_{\langle ij \rangle}, \tag{2.1}$$

which should be understood as the sum over all lattice sites $i$ and all nearest neighbors $j$, where all bonds are counted in both directions. For a quadratic lattice, this means that

$$\sum_{\langle ij \rangle} 1 = \sum_{i} \sum_{\vec{\delta} \in \{a\hat{x}, a\hat{y}\}} 2 = 4N, \tag{2.2}$$

where N is the number of lattice sites. Natural units with the reduced Planck constant $\hbar = 1$, and the Boltzmann constant $k_B = 1$ will be widely used. The lattice constant $a$ will also typically be set equal to 1. Operators in the Schrödinger picture will be denoted as $O$, without any extra indices, while operators in the interaction picture will be written on the form $O_I$.

## 2.2 Cold Atoms and the Bose-Hubbard Model

We start by introducing the physical systems we are interested in and the theoretical model that will be applied in order to describe them.

### 2.2.1 Bose-Einstein Condensation

Atoms are composite particles consisting of protons, neutrons and electrons. Atoms consisting of an even number of such fermionic building blocks are bosons because exchanging an even number of fermions leads to an even number of minus signs. Neutral atoms consist of the same number of electrons and protons, and bosonic atoms therefore need to have an even number of neutrons. Examples of such atoms are the alkali atoms $^{87}$Rb and $^{23}$Na [11]. At low enough temperatures, non-interacting bosonic atoms can macroscopically occupy the ground energy state, as we will see immediately.

Consider a system of non-interacting bosons with single-particle energy levels, $\epsilon_k$, and single-particle dispersion relation $\epsilon_k = ak^b$. Here $k$ is momentum and $a, b$ are constants. The occupation numbers are then, in the grand canonical ensemble, given by the Bose-Einstein distribution

$$n_k = \frac{1}{e^{\beta(\epsilon_k - \mu)} - 1}, \tag{2.3}$$

where $\mu$ is the chemical potential, $\beta = \frac{1}{k_B T}$, $T$ is the temperature of the system and $k_B$ is the Boltzmann constant. Clearly, $\mu$ will always have to be smaller than the ground state energy $\epsilon_0 = 0$ to avoid the possibility of negative occupation numbers. In the thermodynamic limit, the total number of particles is expressed as

$$N = \int_0^\infty \mathrm{d}\epsilon \, D(\epsilon) \frac{1}{e^{\beta(\epsilon - \mu)} - 1}, \tag{2.4}$$

where

$$D(\epsilon) = \sum_{\vec{k}} \delta(\epsilon - \epsilon_k) = D_0 V \epsilon^{\frac{d}{b} - 1}, \tag{2.5}$$

is the density of states. Here $d$ is the dimensionality of the system, $V$ is the $d$-dimensional "volume", $D_0 = \frac{\Omega_d}{(2\pi)^d b a^{d/b}}$ and $\Omega_d$ is the $d$-dimensional solid angle. The expression for $N$ diverges for $\epsilon \to \mu$, and we will therefore have to treat the ground state with special care

$$N = n_0 + D_0 V \int_{0^+}^\infty \mathrm{d}\epsilon \, \frac{\epsilon^{\frac{d}{b} - 1}}{e^{\beta(\epsilon - \mu)} - 1} \equiv n_0 + N_*. \tag{2.6}$$

The number of particles in excited states, $N_*$, is maximized for $\mu = 0$, when it takes the form

$$N_*^{\max} = D_0 V (k_B T)^{d/b} \int_{0^+}^\infty \mathrm{d}x \, \frac{x^{\frac{d}{b} - 1}}{e^x - 1}. \tag{2.7}$$

The integral converges for large $x$, but can diverge for small $x$ where the integrand takes the form $x^{d/b - 2}$ to lowest order in $x$. The integral will therefore converge for $d > b$. When $d$ is not larger than $b$, it is possible to accommodate an unlimited number of particles in the excited states and we do not obtain a macroscopic occupation of the ground state for finite $T$. For free particles with dispersion relation $\epsilon_k = \frac{\hbar^2 k^2}{2m}$, where $m$ is the mass of the particles, we have $b = 2$. It is then possible to have BEC at finite $T$ in three dimensions, but not in two dimensions.

For BEC in low-dimensional systems, trapping potentials are of essential importance [53]. In the case of non-interacting particles in an anisotropic harmonic oscillator potential

$$V(\vec{r}) = \frac{1}{2} m \sum_{i=1}^d \omega_i^2 r_i^2, \tag{2.8}$$

the energy levels are

$$\epsilon(\vec{n}) = \hbar \sum_{i=1}^d n_i \omega_i, \tag{2.9}$$

where the zero-point energy has been neglected and the numbers $n_i$ take on all integer values greater than or equal to zero. It can then be shown that the density of states takes the form [11]

$$D(\epsilon) = \frac{\epsilon^{d-1}}{(d-1)! \prod_{i=1}^{d} \hbar\omega_i}. \tag{2.10}$$

In the case of $d = 2$, we then have $b = 1$ and $d > b$, permitting BEC.

As shown by Bogoliubov [54], the introduction of weak interactions transforms the system into one that can be described as consisting of bosonic quasi-particles with a linear dispersion relation

$$\epsilon_k = c\hbar k, \tag{2.11}$$

in the long-wavelength limit, which can aid the formation of a BEC. The quantity $c$ is the speed of sound at zero temperature.

Going back to equation (2.7), the critical temperature, $T_c$ can be determined by setting $N* = N$ and solving for the temperature, i.e. identifying the temperature where all the particles in the system can no longer be accommodated by the excited states. The result is

$$k_B T_c = \left( \frac{N}{V D_0 \Gamma(\frac{d}{b}) \zeta(\frac{d}{b})} \right)^{b/d}, \tag{2.12}$$

where $\Gamma(x)$ is the gamma function and $\zeta(x)$ is the Riemann zeta function. In the case of free particles in three dimensions, this relation can be rewritten as

$$\rho \lambda_{T_c}^3 = \zeta(3/2) \approx 2.61, \tag{2.13}$$

where $\rho \equiv N/V$ is the density of particles and $\lambda_T \equiv \left(\frac{h^2}{2\pi m k_B T}\right)^{1/2}$ is the thermal de Broglie wavelength. Writing $\rho = \frac{1}{l^3}$, where $l$ is the mean interparticle distance, the condition for condensation implies,

$$\lambda_{T_c} \sim l. \tag{2.14}$$

The result that BEC takes place when the thermal de Broglie wavelength becomes of the order of the interparticle distance is in accordance with the usual understanding that this is the scale where wave functions start to overlap and quantum effects become important. To obtain this regime for a Bose gas, it seems favorable to decrease the temperature and increase the density of the gas. Unfortunately, this would lead to the formation of molecules or the system entering a liquid or solid phase, long before the BEC transition temperature is reached. Gaseous BECs are therefore normally produced at low densities ($10^{13}$ - $10^{15}\,\mathrm{cm}^{-3}$) and extremely low temperatures ($10^{-5}\,\mathrm{K}$ or less) [11].

### 2.2.2 Trapping, Cooling and Tuning

To obtain a condensate, the cold atoms need to be confined in space, isolated from their surroundings. This is achieved through some sort of trapping technique. Magnetic trapping methods exploits the Zeeman effect, i.e. the splitting of atomic energy levels in the presence of a static magnetic field. When placed in an external magnetic field, the energy of an atom in a particular hyperfine state, will either increase or decrease, depending on the specific state. This is due to the interaction between the external magnetic field and the magnetic moment of the electrons and the nucleus, and whether the energy increases or decreases depends on interplay between the electronic and nuclear spin. If

the energy of the state increases, the state is referred to as a *low-field seeker*, and if the energy of the state decreases, the state is reffered to as a *high-field seeker*. When subjected to a spatially inhomogeneous magnetic field, high-field seekers will be attracted to local maxima in the magnetic field, and vice versa. It is not possible to achieve a local maximum in the magnetic field in regions without electrical currents, but it is possible to obtain a local minimum. Magnetic traps can therefore be used to confine atoms in low-field seeking states. The magnetic trap will generally favor a specific hyperfine state and is therefore not well-suited for confinement of atoms in different hyperfine states [11].

Trapping of atoms in different hyperfine states can instead be achieved using a so-called optical trap. In the dipole approximation, the interaction between a neutral atom and an external electric field $\vec{\mathcal{E}}$ is given by

$$H' = -\vec{d} \cdot \vec{\mathcal{E}}, \tag{2.15}$$

where $\vec{d} = q\vec{r}$, is the dipole moment operator and $q$ is charge. The expectation value of the dipole moment operator can be expressed in the position representation as

$$\left\langle \vec{d} \right\rangle = \int \mathrm{d}^3\vec{r}\, \psi(\vec{r})^* (q\vec{r}) \psi(\vec{r}), \tag{2.16}$$

showing the connection to the classical dipole moment when the quantity $q|\psi(\vec{r})|^2$ is identified as the charge density. For a static field, the change in the ground state energy of an atom due to an external electric field is given, to second order in the field, by the quadratic Stark effect

$$\Delta E_g = -\frac{1}{2}\alpha \mathcal{E}^2. \tag{2.17}$$

Here $\alpha$ is the atomic polarizability, given by

$$\alpha = 2\sum_m \frac{\left|\langle m| \vec{d} \cdot \hat{\mathcal{E}} |g\rangle\right|^2}{E_m - E_g}, \tag{2.18}$$

where the sum goes over excited states. Generalizing to a time-dependent electric field with frequency $\omega$, the energy shift takes the form

$$\Delta E_g = -\frac{1}{2}\alpha(\omega) \langle \mathcal{E}(\vec{r}, t)^2 \rangle_t, \tag{2.19}$$

where $\langle \quad \rangle_t$ denotes the time average. The dynamical polarizability is given by [11]

$$\alpha(\omega) = 2\sum_m \frac{(E_m - E_g)\left|\langle m| \vec{d} \cdot \hat{\mathcal{E}} |g\rangle\right|^2}{(E_m - E_g)^2 - (\hbar\omega)^2}. \tag{2.20}$$

Typically, one of the terms in the sum will dominate and the sign of $\alpha(\omega)$ will depend on whether the system is driven above or below the corresponding resonance frequency. If the time-averaged electric field is spatially inhomogeneous, the energy shift can be viewed as a spatially dependent potential

$$V(\vec{r}) = -\frac{1}{2}\alpha(\omega) \langle \mathcal{E}(\vec{r}, t)^2 \rangle_t. \tag{2.21}$$

Using a focused laser beam to create an electric field with a spatial maximum in intensity, it is therefore possible to confine atoms in space by red detuning the laser frequency relative to a resonance frequency of the atoms. Using pairs of counter-propagating laser beams, it is e.g. also possible to produce standing waves, generating a spatially periodic potential

$$V(\vec{r}) = V_0\Big[\sin^2(k_L x) + \sin^2(k_L y)\Big], \tag{2.22}$$

constituting a so-called optical lattice [10, 11]. Here, $k_L$ is the wave vector of the laser and the lattice well depth $V_0$ is proportional to the laser frequency. By adding strong confinement in the $z$-direction, this system imitates a quadratic lattice. Using different laser setups it is possible to generate different types of lattice systems [55, 56].

To lower the temperature of the gas, different types of laser cooling such as Doppler cooling, Sisyphus cooling and Zeeman slowing can be applied. Doppler cooling is much used and can be understood in the following way. Consider an atom subjected to two counter-propagating laser beams with frequency red detuned with respect to an atomic transition between the ground state and an excited state. An atom at rest will then absorb the same amount of right- and left-moving photons and re-emit these in random directions. The atom will then experience no net change in momentum and continue to be at rest. An atom moving e.g. to the right, on the other hand, will, due to the red-detuned laser frequency and the Doppler effect, experience an increased absorption rate for left-propagating photons and a decreased absorption rate for right-propagating photons. Due to the isotropic re-emission, non-stationary atoms will therefore experience a net momentum transfer opposite to their direction of propagation. The particles are therefore slowed down, corresponding to a loss in temperature. Using one pair of lasers for each spatial direction, particles moving in all possible direction can be slowed down. To achieve BEC it is often necessary to further reduce the temperature, using a method called evaporative cooling. The method consists of decreasing the depth of the trap potential, allowing the particles with the most kinetic energy to leave the system, thereby decreasing the average kinetic energy [11].

Interactions in cold atomic gases can usually be described in terms of a single parameter: the scattering length, $a_s$. This is due to large separation between the particles relative to the typical length scale of the interactions, allowing us to only consider two-body collisions, as well as the low kinetic energy of the atoms, making s-wave scattering the dominant interaction mechanism [11]. The scattering length, and therefore also the interaction strength, of the particles can be tuned by taking advantage of Feshbach resonances [57], which appear when the energy of two particles in a scattering process approaches the energy of a bound state of the system, leading to a divergence of the scattering length. Close to such a resonance, the scattering length can be expressed on the form [11]

$$a_s \propto \frac{1}{E - E_{res}}. \tag{2.23}$$

The difference in energy between the incoming particles and the bound state can typically be altered by an external magnetic field, thereby influencing the scattering length of the particles.

### 2.2.3 Multicomponent Bose-Hubbard Model

As mentioned in the introduction, we will focus on a three-component system without component-mixing interactions. A condensate of this type that is adiabatically loaded into a $d$-dimensional cubic lattice can be described by a Bose-Hubbard model on the form [58–60]

$$H = -t \sum_{\langle ij \rangle \sigma} a_{i\sigma}^\dagger a_{j\sigma} + \frac{1}{2} \sum_{i\sigma\sigma'} U_{\sigma\sigma'} n_{i\sigma} (n_{i\sigma'} - \delta_{\sigma\sigma'}) - \sum_{i\sigma} \mu_\sigma n_{i\sigma}. \tag{2.24}$$

where $\sigma \in \{a, b, c\}$ and

$$U_{\sigma\sigma'} = U \begin{pmatrix} 1 & \lambda_{ab} & \lambda_{ac} \\ \lambda_{ab} & 1 & \lambda_{bc} \\ \lambda_{ac} & \lambda_{bc} & 1 \end{pmatrix}. \tag{2.25}$$

Here $a_{i\sigma}^\dagger$ is a creation operator, creating a particle of type $\sigma$ at lattice site $i$, $t$ is the hopping amplitude, $U_{\sigma\sigma'}$ is the on-site component-dependent interaction coefficient, $n_{i\sigma} \equiv a_{i\sigma}^\dagger a_{i\sigma}$ is the number operator, $\delta_{\sigma\sigma'}$ is the Kronecker delta, $\mu_\sigma$ is the component-dependent chemical potential, $U$ is the intracomponent interaction strength, which will be assumed to be positive in the following, and $\lambda_{\sigma\sigma'}$ is the relative inter- to intracomponent interaction strength (often just referred to as the intercomponent interaction strength) between the components $a$ and $b$. We have assumed that the intracomponent interaction strengths are equal. In the cases where also the intercomponent interactions strengths are equal, we will set $\lambda \equiv \lambda_{ab} = \lambda_{ac} = \lambda_{bc}$.

The model can be derived by starting from the second quantized Hamiltonian

$$\begin{aligned} H = &\sum_b \int \mathrm{d}\vec{r}\, \Psi_b^\dagger(\vec{r}) \left[ \frac{\vec{p}^2}{2m} + V(\vec{r}) \right] \Psi_b(\vec{r}) \\ &+ \frac{1}{2} \sum_{bb'cc'} \int \mathrm{d}\vec{r} \mathrm{d}\vec{r}'\ \Psi_b^\dagger(\vec{r}) \Psi_{b'}^\dagger(\vec{r}') U(\vec{r} - \vec{r}') \Psi_{b'}(\vec{r}') \Psi_b(\vec{r}), \end{aligned} \tag{2.26}$$

where the indices of the field operators correspond to the different components of the system and non-component conserving interactions have been neglected. The next step is to introduce a component-dependent, effective contact potential

$$U(\vec{r} - \vec{r}') = \widetilde{U}_{bb'}\, \delta(\vec{r} - \vec{r}'), \tag{2.27}$$

and expanding the field operators in the Wannier basis

$$\Psi_b(\vec{r}) = \sum_{i\sigma} \omega(\vec{r} - \vec{r_i}) \chi_\sigma(b) a_{i\sigma}. \tag{2.28}$$

Here, $\chi_\sigma$ takes care of the internal degree of freedom and $a_{i\sigma}$ is then the annihilation operator for bosons of component $\sigma$ in the Wannier state, associated with the lowest Bloch band, localized around $\vec{r}_i$. The Wannier functions constitute a complete set of approximately localized single-site eigenstates constructed from a superposition of Bloch functions, effectively trading off localization in energy for localization in space [61]. Working out the details, neglecting small terms and including a chemical potential term, the Hamiltonian takes the form of equation (2.24) with

$$\begin{aligned} t \quad &= -\int \mathrm{d}\vec{r}\, \omega^*(\vec{r} - \vec{r}_i) \left( \frac{\vec{p}^2}{2m} + V(\vec{r}) \right) \omega(\vec{r} - \vec{r}_{i+\delta}), \\ U_{\sigma\sigma'} &= \widetilde{U}_{\sigma\sigma'} \int \mathrm{d}\vec{r}\, |\omega(\vec{r} - \vec{r}_i)|^4. \end{aligned} \tag{2.29}$$

In addition to the chemical potential term, governing the particle numbers, the model consists of two terms: the hopping term and the interaction term. The hopping term introduces tunneling between nearest-neighbor lattice sites, while the interaction term simply captures the short-range interactions between atoms that are located at the same lattice site. Depending on the relative strength of these two terms, the system can be in a superfluid phase or a Mott-insulating phase. We will discuss these briefly in the 1-component case where the Hamiltonian takes the form [62]

$$H = -t \sum_{\langle ij \rangle} a_i^\dagger a_j + \frac{U}{2} \sum_i n_i(n_i - 1) - \mu \sum_i n_i. \tag{2.30}$$

In the Mott-insulating phase, the particles are localized at individual lattice sites and the system can be described in terms of a many-particle state

$$|\Psi\rangle \propto \prod_{i=1}^{N} (a_i^\dagger)^n |0\rangle , \tag{2.31}$$

where $n$ is the number of particles per lattice site. The Mott-insulating phase takes place at small $t/U$ and in the limit $t/U \to 0$, the Hamiltonian simplifies to

$$H = \frac{U}{2} \sum_i \ n_i(n_i - 1) - \mu \sum_i n_i. \tag{2.32}$$

All sites are equivalent and the temperature is very close to zero. We can therefore analyze the system by examining the energy of the one-site problem,

$$E = \frac{U}{2} n(n-1) - \mu n. \tag{2.33}$$

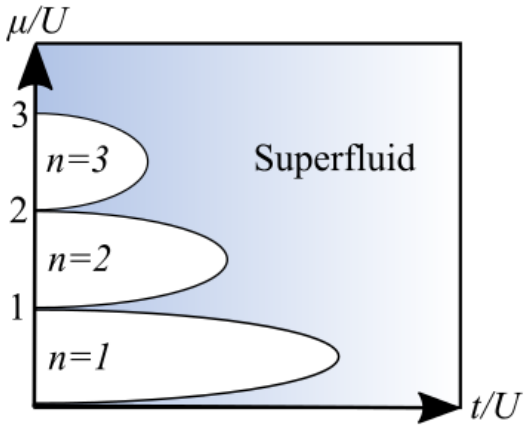


Figure 2.1: Qualitative phase diagram of the Bose-Hubbard model with repulsive on-site interaction, showing the Mott insulator lobes, with $n$ localized particles per lattice site, and the superfluid phase.

For $n = 0, 1$, the first term vanishes and for small, but nonzero, chemical potential the case of $n = 1$ is energetically favorable. For increasing values of $\mu$, $n = 1$ is still energetically favorable until we reach

the point where the energy that is gained from the second term by changing $n$ from 1 to 2 becomes larger than the energy that is lost in the first term. In this way, the favored value of $n$ increases in steps for increasing chemical potential. The values for $\mu/U$ where these steps take place can easily be worked out from equation (2.33).

In the limit $t/U \to \infty$, the particles are completely delocalized and the system is in a superfluid phase. The many-body ground state can be expressed on the form [62]

$$|\Psi\rangle \propto \left( \sum_{m=1}^{M} a_m^\dagger \right)^N |0\rangle \,, \tag{2.34}$$

where $N$ is the number of lattice sites, and $M$ is the number of particles, controlled by the chemical potential. Between these two phases there is a quantum phase transition. The phase diagram depends on e.g. the dimensionality of the lattice, but it takes the qualitative form shown in figure 2.1 [63]. In this thesis we will be interested in the superfluid phase.

## 2.3 Superfluids

The most striking characteristic of a superfluid is the lack of viscosity which enables the superfluid to flow through narrow pipes without friction and climb out of unsealed containers [35]. In addition, superfluids generally also display other interesting effects such as the fountain effect [64], where superfluid helium flows through a capillary in the direction of increasing temperature [35]. Stirring a superfluid leads to the formation of quantized vortices [65]. Such vortices are characterized by the absence of superfluid density at the center and circular superfluid flow around it, carrying a quantized angular momentum [11]. In three dimensions, the superfluid rotates around so-called vortex lines that either form loops or end at the system boundaries, while two-dimensional superfluids have circular currents flowing around point singularities [35].

Superfluidity was first observed in liquid $He^4$ [66, 67]. While liquids normally become solids at low temperatures, Helium stays in its liquid form all the way down to zero temperature for sufficiently low pressure (below 25 atm [65]). This trait is due to the low mass of the helium atoms which, helped by the weak interatomic interactions, makes the zero-point kinetic energy large enough to combat crystal formation [11, 35]. The transition to a superfluid phase takes place at the so-called lambda point, $T_\lambda = 2.17\,\mathrm{K}$ (at 1 atm), where the specific heat of the fluid diverges. The name comes from the fact that the specific heat as a function of temperature forms a curve that looks like the Greek letter lambda [68].

As proposed by Landau [69], superfluidity is somewhat related to BEC, but the relation is not as clear as one might expect. An example is that $He^4$ at low temperatures becomes completely superfluid while only about 10% of the particles are part of the condensate [11]. It is also possible to have a superfluidity completely without BEC, as observed in superfluid films [70] where interacting bosons in two dimensions become superfluid, as described by the BKT theory [71], without the formation of a condensate [53]. Starting with the description of a condensate is, however, still a useful approach for investigation of superfluid systems.

Tisza [72] and Landau [69] introduced the useful phenomenological understanding of a superfluid as consisting of two parts: a normal part and a superfluid part. Microscopically, one can construct such a model by considering a superfluid as a combination of a condensate and elementary excitations. The condensate then contains the superfluid part while the normal part arises from the elementary

excitations. As we saw in section 2.2.1, e.g. the particle density of the Bose gas divided itself naturally into a contribution from the condensed particles and a contribution from the elementary excitations. A condensate that refuses to interact with its surroundings will clearly flow without friction. The question is then under which conditions the system rejects excitations from the surroundings and thus avoids dissipation of kinetic energy. Landau provided a general criterion that the excitations need to fulfill in order for superfluidity to take place.

### 2.3.1 The Landau Criterion

Consider a liquid that in some reference frame has energy $E = E_0 + E(\vec{P})$ and momentum $\vec{P}$. In the reference frame moving with some velocity $\vec{v}$, relative to the original frame, the energy of the system is then given by

$$E'(\vec{v}) = E - \vec{P} \cdot \vec{v} + \frac{1}{2} M v^2, \tag{2.35}$$

where $M$ is the mass of the liquid. Consider now a condensate that flows around an obstacle. We take the frame of the condensate to be the original frame, in which the obstacle moves through the condensate with velocity $\vec{v}$. The argument can be generalized to the case of non-vanishing initial excitations [11], but, for simplicity, we will use a condensate as our starting point. In the frame of the obstacle, the energy of the system is now

$$E'(\vec{v}) = E_0 + \frac{1}{2} M v^2, \tag{2.36}$$

since the condensate has zero momentum in the original frame. If we now introduce some excitation of momentum $\vec{p}$, the energy in the original frame is

$$E = E_0 + \epsilon_p \tag{2.37}$$

and the energy in the reference frame of the obstacle is

$$E'(\vec{v}) = E_0 + \epsilon_p - \vec{p} \cdot \vec{v} + \frac{1}{2} M v^2. \tag{2.38}$$

In the rest frame of the obstacle, the obstacle is unable to transfer any energy to the fluid. For the excitation to be energetically favorable, we therefore need to have

$$\epsilon_p - \vec{p} \cdot \vec{v} < 0. \tag{2.39}$$

The smallest $v$ that satisfies this criterion is called the Landau critical velocity and is then given by

$$v_c = \min_p \left\{ \frac{\epsilon_p}{p} \right\}. \tag{2.40}$$

For $v$ less than the Landau critical velocity it is not possible to create excitations, meaning that the fluid can flow with velocity less than $v$, relative to the obstacle, without dissipative effects. Whether superfluidity is possible or not is then determined by the nature of the elementary excitations. For free particles with $\epsilon_p = \frac{p^2}{2m}$, the critical velocity vanishes and it is always possible to produce excitations. In the case of Bogoliubov's weakly interacting Bose gas, on the other hand, the critical

velocity becomes the speed of sound at zero temperature that was introduced in equation (2.11). A non-interacting Bose gas in three dimensions would thus be an example of a system that could condense without superfluidity, while a weakly interacting Bose gas in one dimension (at least according to the Landau criterion [73]) can be superfluid without the presence of a BEC.

### 2.3.2 Classical Field Description

Building on the ideas of Einstein [35, 74], a superfluid system can, at least under certain conditions, be described in terms of a classical complex field. Following the prescription in [35], we start with a relativistic field $\Psi(\vec{r}, t)$ that satisfies the Klein-Gordon equation

$$\frac{\partial^2 \Psi}{\partial t^2} = c^2 \nabla^2 \Psi - \lambda^2 \Psi, \tag{2.41}$$

where $c$ is the speed of light and $\lambda$ is a real parameter. The motivation for this starting point is that the Klein-Gordon equation is the simplest Lorentz invariant equation that allows for wave-propagation with velocity less than the speed of light. Investigating the non-relativistic limit, one can write the field on the form

$$\Psi(\vec{r}, t) = \psi(\vec{r}, t) e^{-i\lambda t}, \tag{2.42}$$

and show that the Klein-Gordon equation reduces to

$$i\frac{\partial \psi}{\partial t} = -\frac{c^2}{2\lambda} \nabla^2 \psi. \tag{2.43}$$

Starting from the simplest possible solution $\psi = \sqrt{n}$, which does not evolve in time, and examining how the complex field $\Psi(\vec{r}, t)$ transforms under a Galilean transformation, the field describing a uniform flow with velocity $\vec{v}$, takes the form

$$\psi(\vec{r}, t) = \sqrt{n} e^{i\phi(\vec{r}, t)}, \tag{2.44}$$

where the velocity is related to the gradient of the phase through

$$\vec{v} = \gamma \nabla \phi, \tag{2.45}$$

and $\gamma = c^2/\lambda$. Generalizing to the case of non-uniform flow, the velocity is defined to be related to the gradient of the phase in the same way. It should be noted that the quantity $n = |\psi|^2$, ought to be referred to as the matter density, rather than the particle density, as the concept of individual particles should be avoided at the classical field level. The non-relativistic version of the Klein-Gordon equation also follows from the Hamiltonian functional

$$H = \frac{\gamma}{2} \int \mathrm{d}^d r |\nabla \psi|^2, \tag{2.46}$$

through normal Hamiltonian mechanics where the scalar field $\psi$ is a complex canonical variable

$$i\frac{\partial \psi}{\partial t} = \frac{\delta H[\psi, \psi^*]}{\delta \psi *}. \tag{2.47}$$

Superfluidity can then be produced by introducing a interaction term and an inhomogeneous potential term in the Hamiltonian, preserving the U(1) symmetry,

$$H = \int \mathrm{d}^d r \left[ \frac{\gamma}{2} |\nabla \psi|^2 + \frac{g}{2} |\psi|^4 + \mathcal{V}(\vec{r}) |\psi|^2 \right], \tag{2.48}$$

where $g$ is a positive interaction parameter. The role of the interaction term is to ensure that the superfluid has a uniform density distribution in the bulk, even in the presence of boundary conditions. Equation (2.47) now produces

$$i \frac{\partial \psi}{\partial t} = -\frac{\gamma}{2} \nabla^2 \psi + g |\psi|^2 \psi + \mathcal{V}(\vec{r}) \psi, \tag{2.49}$$

which is the time-dependent Gross-Pitaevskii equation (GPE). This equation has solutions

$$\psi = \sqrt{n} e^{i\phi}, \tag{2.50}$$

that feature superfluidity with the same relationship between the velocity and the gradient of the phase as obtained earlier. The superfluid features can be revealed by imagining a system confined within a torus. The GPE is a second-order differential equation in spatial coordinates, and, assuming that $|\psi| \neq 0$ everywhere inside the torus, the field needs to be a smooth function of spatial coordinates. This, in turn, tells us that the gradient of the phase and the closed line integral

$$I = \oint_C \mathrm{d}\vec{l} \cdot \nabla \phi = 2\pi M, \tag{2.51}$$

are well defined. The quantity $M$ is here an integer, and the result naturally follows from the fact that the field needs to return to its original value. Considering a non-trivial contour that encircles the hole of the torus, it is then possible to have $M \neq 0$. As long as $|\psi| \neq 0$, the function $I(t)$ should be a continuous function of time, and since $I(t)$ takes on discrete values, it is therefore conserved. According to equation (2.45), a solution with $M \neq 0$ then exhibits a persistent current flowing along the contour, i.e. a superflow.

In the quantum mechanical treatment the quantity $\gamma$ becomes $\gamma = \hbar/m$, where we for once have included the $\hbar$. The earlier mentioned vortices can now be understood in terms of winding of the phase $\phi$ around points with $|\psi| = 0$. The circulation around a vortex is then given by

$$\oint_C \mathrm{d}\vec{l} \cdot \vec{v} = \frac{\hbar}{m} \oint_C \mathrm{d}\vec{l} \cdot \nabla \phi = \frac{2\pi\hbar}{m} s \tag{2.52}$$

where $s$ is the number of times the phase winds around the vortex axis, in the positive direction. In the case of several components there will also be several fields and several phases $\phi_\alpha$, which could all wind around a vortex axis. A general vortex is then expressed on the form $(s_a, \ldots, s_l)$, where $l$ is the number of components. A vortex where more than one of the phases have nonzero winding is called a composite vortex, as opposed to an elementary vortex. The presence of vortices means that the line integral in equation (2.51) might no longer be conserved. Vortices that cross the contour can change the value of the integral and impact or completely destroy the superfluidity.

### 2.3.3 Twisted Boundary Conditions

The effect of a gauge field $\vec{A}$, can be included by taking $\nabla \to \nabla - i\vec{A}$, in the Hamiltonian in equation (2.48), and the relationship between the velocity and the gradient of the phase can be shown to be given by

$$\vec{v} = \gamma(\nabla\phi - \vec{A}). \tag{2.53}$$

In a simply connected system, e.g. a system with hard-wall boundary conditions, a vector potential without curl and time-dependence can be gauged away by a standard gauge transformation $\vec{A}' = \vec{A} - \nabla\chi$, leading to

$$\phi' = \phi - \chi, \tag{2.54}$$

with

$$\chi(\vec{r}) = \int\limits_{C(\vec{r},\vec{r}_0)} \mathrm{d}\vec{l}\cdot\vec{A}. \tag{2.55}$$

Here $C(\vec{r},\vec{r}_0)$ is a path from some defined point $\vec{r}_0$ to $\vec{r}$. On the other hand, in systems with periodic boundary conditions, it is possible to have paths that wind around the system in some direction, similar to the type we considered for the case of a toroidal geometry. For such a path, taking $L$ to be the length of the system in the relevant direction, we have

$$\chi(L) = \oint\limits_{C} \mathrm{d}\vec{l}\cdot\vec{A} = \widetilde{\chi} + 2\pi M, \tag{2.56}$$

while

$$\chi(0) = 0, \tag{2.57}$$

implying, in general,

$$\phi'(L) - \phi'(0) \neq 2\pi M, \tag{2.58}$$

which is not consistent with the single-valuedness of the field $\psi$. The gauge field does, in other words, give rise to physical effects that we cannot simply ignore. For a homogeneous system with a periodic boundary in the $x$-direction and an external gauge field

$$\vec{A} = -\frac{\chi_0}{L}\hat{x}, \tag{2.59}$$

attempting to gauge out the vector potential produces the relation

$$\psi(x + L) = e^{i\chi_0}\psi(x). \tag{2.60}$$

The system is then said to have *twisted boundary conditions*, and $\chi_0$ is referred to as a phase twist. From equation (2.53) we also see that the introduction of the gauge field transform a system at rest into a system flowing with velocity

$$\vec{v} = \gamma \frac{\chi_0}{L} \hat{x}. \tag{2.61}$$

As we will see later, this can be utilized to define the superfluid drag density in terms of the system's response to such a gauge field. This method does not rely on Galilean invariance, which is not present in a system on a lattice since the lattice defines a preferred reference frame [75].

### 2.3.4 Hydrodynamics of Multicomponent Superfluids

Returning to Landau's two-fluid picture, the free energy density of a superfluid system is given by

$$f = f_0 + \frac{1}{2}(\rho_n v_n^2 + \rho_s v_s^2), \tag{2.62}$$

where $f_0$ is the energy density of the system at rest, $\rho_n$ is the density of the normal component and $\rho_s$ is the density of the superfluid component. In the two-component case, the expression for the free energy density of the superfluid takes the form [33]

$$f_s = \frac{1}{2}(\rho_a - \rho_{ab})v_a^2 + \frac{1}{2}(\rho_b - \rho_{ab})v_b^2 + \rho_{ab}\vec{v}_a \cdot \vec{v}_b, \tag{2.63}$$

in the hydrodynamic limit. The quantity $\rho_a$ is the total superfluid density of the $a$-component, $\rho_{aa} \equiv \rho_a - \rho_{ab}$ is the superfluid density of component $a$ carried by the superflow of component $a$, while $\rho_{ab}$ is the superfluid drag density, which is the superfluid density of component $a$ carried by the superfluid motion of component $b$ (or the other way around). The superfluid density currents are obtained by differentiating the free energy density with respect to the respective superfluid velocities, producing

$$\begin{aligned} \vec{j}_a &= (\rho_a - \rho_{ab})\vec{v}_a + \rho_{ab}\vec{v}_b \\ \vec{j}_b &= (\rho_b - \rho_{ab})\vec{v}_b + \rho_{ab}\vec{v}_a. \end{aligned} \tag{2.64}$$

Considering the case where only one of the components has a non-zero superfluid velocity, we see that the other component will have an induced current with direction relative to the original current depending on the sign of the superfluid drag density. A positive superfluid drag density leads to so-called co-flow (entrainment), while a negative superfluid drag density leads to counter-flow [47]. The superfluid drag density will often just be referred to as the drag.

In the three-component case, the expression for the free energy density of the superfluid is generalized to

$$\begin{aligned} f_s = &\frac{1}{2}(\rho_a - \rho_{ab} - \rho_{ac})v_a^2 + \frac{1}{2}(\rho_b - \rho_{ab} - \rho_{bc})v_b^2 + \frac{1}{2}(\rho_c - \rho_{ac} - \rho_{bc})v_c^2 \\ &+ \rho_{ab}\vec{v}_a \cdot \vec{v}_b + \rho_{ac}\vec{v}_a \cdot \vec{v}_c + \rho_{bc}\vec{v}_b \cdot \vec{v}_c. \end{aligned} \tag{2.65}$$

This free energy density can be compactly rewritten as [34]

$$f_s = \frac{1}{2}\vec{V}^T \rho \vec{V}, \tag{2.66}$$

where $\vec{V}^T = (\vec{v}_a, \vec{v}_b, \vec{v}_c)$ and

$$\rho = \begin{pmatrix} \rho_{aa} & \rho_{ab} & \rho_{ac} \\ \rho_{ba} & \rho_{bb} & \rho_{bc} \\ \rho_{ca} & \rho_{cb} & \rho_{cc} \end{pmatrix}. \tag{2.67}$$

Here we have $\rho_{\beta\alpha} = \rho_{\alpha\beta}$. The superfluid density currents then become

$$\vec{J} = \rho\vec{V}, \tag{2.68}$$

where $\vec{J}^T = (\vec{j}_a, \vec{j}_b, \vec{j}_c)$. Written out, the respective superfluid density currents take the form

$$\begin{aligned} \vec{j}_a &= (\rho_a - \rho_{ab} - \rho_{ac})\vec{v}_a + \rho_{ab}\vec{v}_b + \rho_{ac}\vec{v}_c \\ \vec{j}_b &= (\rho_b - \rho_{ab} - \rho_{bc})\vec{v}_b + \rho_{ab}\vec{v}_a + \rho_{bc}\vec{v}_c \\ \vec{j}_c &= (\rho_c - \rho_{ac} - \rho_{bc})\vec{v}_c + \rho_{ac}\vec{v}_a + \rho_{bc}\vec{v}_b. \end{aligned} \tag{2.69}$$

For a system on a lattice, the superfluid drag density generally becomes a tensor $\rho_{ab}^{\alpha\beta}$, where $\alpha$ and $\beta$ denote lattice directions. However, for the case of a $d$-dimensional cubic lattice we have $\rho_{ab}^{\alpha\beta} = \rho_{ab}\delta_{\alpha\beta}$, and the free energy can be expressed in the same way as before [50].

## 2.4 Monte Carlo Methods

*Monte Carlo methods* are procedures that are characterized by their utilization of repeated random sampling. Such methods are often used to solve problems that do not initially contain any notion of randomness, but where the introduction of randomness simplifies the problem or provides a faster solution. A common example of the principle of Monte Carlo methods is to estimate the value of $\pi$ by randomly picking points within the unit square of area 1 and counting the fraction of points that end up within the unit circle of area $\pi/4$. Multiplying this fraction by 4, one obtains an estimate of $\pi$.

### 2.4.1 Monte Carlo Integration

Numerical integration in one dimension can be performed in a deterministic fashion by dividing the area under the curve into small parts, taking samples to estimate the area of these parts, and summing up the total volume. The same general method can be applied to calculate multidimensional integrals, but, as the number of dimensions increases, the error in the estimate scales less favorably with the number of samples [76]. The error, $\sigma_N$, might e.g. depend on the number of samples, $N$, and the number of dimensions, $d$, in the following way: $\sigma_N \propto N^{-2/d}$, as illustrated for different values of $d$ in figure 2.2.

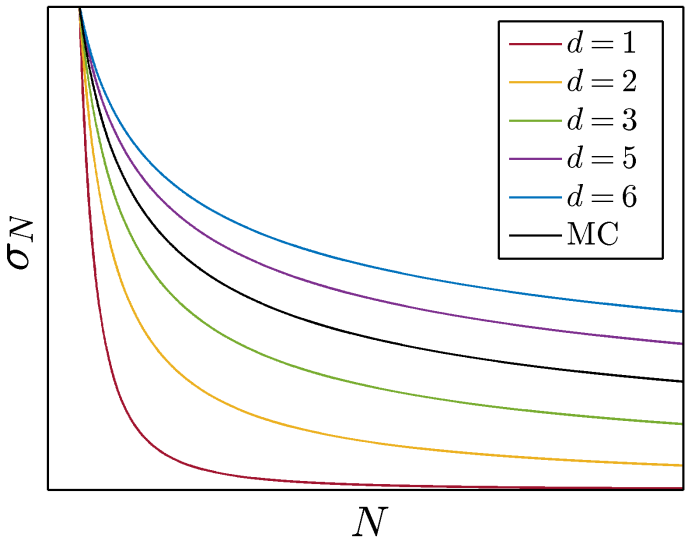


Figure 2.2: Example of scaling of the error in the result of numerical integration with regard to the number of samples, $\sigma_N \propto N^{-2/d}$, shown for different integral dimensionalities. The error in Monte Carlo estimates (black curve) is independent of the number of dimensions.

An alternative approach is to randomly sample points in parameter space to estimate the average value of the function of interest. Multiplying this average with the total volume of the parameter space produces an estimate of the desired integral, $I$, [77]

$$I \equiv \int_V \mathrm{d}\vec{r}\, f(\vec{r}) = V\,\hat{f} \approx V\,\overline{f} = V\frac{1}{N}\sum_{i=1}^{N} f(\vec{r}_i), \tag{2.70}$$

where $\vec{r}$ is a $d$-dimensional vector and $V$ is a $d$-dimensional "volume" and we have used $\hat{f}$ to denote the true mean of the function $f$. This method is called *Monte Carlo Integration*. The advantage of Monte Carlo integration is that the error in the estimate scales as $1/\sqrt{N}$, regardless of the dimensionality of the integral [76]. This follows from the central limit theorem, which tells us that the sample mean follows a Gaussian distribution with variance $\sigma^2/N$, for suffciently large N [78]. Here $\sigma$ is the standard deviation of the population we are taking the mean over, which in our case is the function $f(\vec{r})$ for $r \in V$. We will refer to this standard deviation as the standard deviation of the function $f$ over $V$, defined as [76]

$$\sigma_f = \sqrt{\frac{1}{V}\int_V \mathrm{d}\vec{r}\left(f(\vec{r}) - \hat{f}\right)^2}. \tag{2.71}$$

The error in the Monte Carlo estimate is then

$$\sigma_N = V\frac{\sigma_f}{\sqrt{N}}, \tag{2.72}$$

independently of the number of dimensions, making Monte Carlo integration the preferred method for high-dimensional integrals. For statistically independent samples, randomly generated from a uniform distribution, the error can be estimated as [78]

$$\xi_N = \frac{V}{\sqrt{N}}\sqrt{\frac{\sum_{i=1}^{N}\left(f(\vec{r}_i) - \overline{f}\right)^2}{(N-1)}} = V\sqrt{\frac{\overline{f^2} - \overline{f}^2}{N-1}}. \tag{2.73}$$

Generating the sample points from a uniform distribution can be suitable in cases where the function of interest does not vary much over the volume of integration, but if the integral is e.g. dominated by contributions from a very small part of the total volume of integration, it will take an immense amount of samples to resolve the details of the region that actually matters. This problem can be addressed through *importance sampling*, which relies on sampling the dominating parts of the volume of integration more often than the "less important" parts. Rewriting the integral and picking out random points in the volume of integration according to a non-negative definite and normalized probability distribution $p(\vec{r})$, the integral can be estimated as [78]

$$I = \int_V \mathrm{d}\vec{r}\, f(\vec{r}) = \int_V \mathrm{d}\vec{r}\, p(\vec{r})\frac{f(\vec{r})}{p(\vec{r})} \approx \frac{1}{N}\sum_{i=1}^{N}\frac{f(\vec{r}_i)}{p(\vec{r}_i)}. \tag{2.74}$$

This method consists of nothing more than to sample some parts of the volume of integration more often, and, to avoid changing the value of the integral, these samples will then have to be weighted less than samples from the regions that are less frequently sampled. The weighting simply means that instead of taking $n$ samples from an "unimportant" region and adding them to the total sum, we can take e.g. $n/2$ samples and multiply the values by 2, pretending that we took $n$ samples. For an "important" region we can, instead of taking $n$ samples, take e.g. $2n$ samples and divide the values by 2, pretending that we only took n samples. This clearly does not change the value of the integral and can improve the resolution of the regions that contribute most to the integral.

Choosing a uniform distribution accounts to setting $w(\vec{r})$ equal to 1 in

$$p(\vec{r}) = \frac{w(r)}{\int_V \mathrm{d}\vec{r}\, w(\vec{r})}, \tag{2.75}$$

leading to $p(\vec{r}) = 1/V$. Plugging this into equation (2.74) reproduces the result in equation (2.70), showing why there is no factor $V$ in equation (2.74). The potential improvement of generating samples from some non-uniform probability distribution can be determined by investigating the standard deviation of the function $f(\vec{r})/p(\vec{r})$ over the transformed volume of integration, given by [78]

$$\sigma_{f/p} = \sqrt{\int_V \mathrm{d}\vec{r}\, p(\vec{r}) \left[\frac{f(\vec{r})}{p(\vec{r})}\right]^2 - \left[\int_V \mathrm{d}\vec{r}\, p(\vec{r}) \frac{f(\vec{r})}{p(\vec{r})}\right]^2} = \sqrt{\int_V \mathrm{d}\vec{r}\, \frac{[f(\vec{r})]^2}{p(\vec{r})} - I^2}. \tag{2.76}$$

For a non-negative definite function $f(\vec{r})$, this expression is minimized by choosing

$$p(\vec{r}) = \frac{f(\vec{r})}{\int_V \mathrm{d}\vec{r}\, f(\vec{r})} = \frac{f(\vec{r})}{I}, \tag{2.77}$$

which, in fact, eliminates the standard deviation completely, which will, in turn, eliminate the error in the estimate of the integral, $\sigma_{f/p}/\sqrt{N}$ [76]. That this choice of $p(\vec{r})$ would, in fact, always give us the correct answer can be seen from plugging this $p(\vec{r})$ into equation (2.74). We then obtain an expression consisting of the correct result for the integral, i.e. $I$, multiplied by a sum that is just the average of 1, providing the same result regardless of the number of sample points. The obvious complication is that $I$ is the unknown quantity we are trying to calculate. In practice we therefore have to try to pick a normalized distribution $p(\vec{r})$ that resembles $f(\vec{r})$ in order to improve the precision of our estimate. In our applications of this method, we will be interested in the fraction of two similar integrals and find a way to avoid calculating the relevant normalization constant. Being able to obtain an exact result from only one sample is, however, still too much to ask for.

### 2.4.2 Monte Carlo Integration in Classical Statistical Mechanics

Multidimensional integrals, or sums, of major interest in statistical mechanics are *the partition function*,

$$Z = \int \mathscr{D}C\, e^{-\beta H[C]}, \tag{2.78}$$

and the related *thermal average*

$$\langle O \rangle = \frac{1}{Z} \int \mathscr{D}C\, O[C]\, e^{-\beta H[C]}, \tag{2.79}$$

here presented in their classical and continuous form for the canonical ensemble. The integral covers the phase space of the system in question, a configuration is denoted by $C$, and $O$ is some physical quantity of interest. We will generally focus on classical physics, for the time being, because we, at a later point, will map the quantum system described in beginning of the chapter to a classical system in order to perform Monte Carlo simulations.

Performing uniform random sampling, the Monte Carlo estimate of the thermal average of the quantity $O$ is, following the procedure of the previous section, expressed as

$$\langle O \rangle_{\mathrm{MC}} = \frac{\sum_{i=1}^{N} O[C_i]\, e^{-\beta H[C_i]}}{\sum_{i=1}^{N} e^{-\beta H[C_i]}}, \tag{2.80}$$

where the prefactor, earlier denoted as $V/N$, in the nominator has been cancelled out by the same factor in the denominator. If we instead perform importance sampling according to the canonical distribution function $\frac{1}{Z}\, e^{-\beta H[C]}$, the expression simplifies to

$$\langle O \rangle_{\mathrm{MC}} = \frac{1}{N} \sum_{i=1}^{N} O[C_i], \tag{2.81}$$

where the normalization factor $Z$ has been conveniently cancelled out. We therefore, for the time being at least, do not have to worry about calculating the actual value of $Z$. The reminding issue is, however, that we need to be able to generate random configurations, $C_i$, according to the canonical distribution function where the unknown $Z$ appears once again. This problem will be tackled by means of Markov chains.

One should, at this point, notice the similarity between the outlined procedure and how one would, ideally, establish the thermal average of a given quantity in an experiment. In such an experiment, given that it would be possible to measure the quantity of interest by taking a snapshot of the state of the system, the thermal average would be determined by sampling an infinite number of equally macroscopically prepared systems and simply calculating the average value. Each state the system could be in would then be sampled with frequency according to the weighting function, just like in our Monte Carlo scheme. We are, in other words, simply trying to mimic such an ideal experimental determination of the thermal average.

### 2.4.3 Markov Chains

A *Markov chain* can be said to be a stochastic model describing the evolution of the distribution of a random variable in a memoryless process. For our purposes, the random variable will be the state of our system, and the memorylessness simply means that knowledge of the probability distribution of the state of our system at any given point in the process is sufficient for predicting the future evolution of the distribution. Consider a system that can initially be described by a probability vector defined in the following way [78]

$$\vec{\pi}^{(0)} = (\pi_1^0, \pi_2^0, \ldots, \pi_n^0). \tag{2.82}$$

Here, the indices of the components correspond to different states the system could be in, and the components $\pi_i^{(0)}$ represent the probability for the system to be in each of these states at the initial point in the sequence. If the initial state of the system is known, we just have e.g. $\vec{\pi}^{(0)} = (1, 0, \ldots, 0)$. The probabilities for finding the system in the different states at the next point in the process are described by the probability vector $\vec{\pi}^{(1)} = (\pi_1^1, \pi_2^1, \ldots, \pi_n^1)$, which is related to the initial one by the *transition matrix*, $\mathcal{P}$, in the following way

$$\vec{\pi}^{(1)} = \vec{\pi}^{(0)} \mathcal{P}. \tag{2.83}$$

The matrix element $\mathcal{P}_{ij}$ should be understood as the probability for the system to transition from state $i$ to state $j$. In general, the transition probabilities between different states could depend on the total number of steps that have been performed. This would not destroy the memorylessness of the process [79]. We will, however, focus on so-called stationary processes, where all the elements $\mathcal{P}_{ij}$ in

$$\mathcal{P} = \begin{pmatrix} \mathcal{P}_{11} & \mathcal{P}_{12} & \dots & \mathcal{P}_{1n} \\ \mathcal{P}_{21} & \mathcal{P}_{22} & \dots & \mathcal{P}_{2n} \\ \vdots & \vdots & \ddots & \vdots \\ \mathcal{P}_{n1} & \mathcal{P}_{n2} & \dots & \mathcal{P}_{nn} \end{pmatrix}, \tag{2.84}$$

are constant quantities for a given system. Moreover, $\mathcal{P}$ is a stochastic matrix, satisfying

$$\mathcal{P}_{ij} \geq 0, \tag{2.85}$$

and

$$\sum_{j=1}^{n} \mathcal{P}_{ij} = 1, \tag{2.86}$$

meaning simply that the transition probabilities cannot be negative and that probability is conserved. The probability distribution of states at a later point in the process are now generated by repeated multiplication with the transition matrix, giving

$$\vec{\pi}^{(r)} = \vec{\pi}^{(0)} \mathcal{P}^{\,r}. \tag{2.87}$$

Consider now the case where $n$ is a finite number, meaning that the number of possible states our system can occupy is finite. If the Markov process, in this case, is ergodic, i.e. all states of the system can be reached from all other states by a finite number of steps, the *limiting distribution*

$$\vec{\pi} = \lim_{r \to \infty} \vec{\pi}^{(0)} \mathcal{P}^{\,r}, \tag{2.88}$$

exists, and it is independent of the initial distribution [78]. Moreover, the limiting distribution is a *stationary distribution*,

$$\vec{\pi} \mathcal{P} = \vec{\pi}. \tag{2.89}$$

and it is also unique [80]. The case where the number of possible states is countably infinite is more complicated, but typically, we will still have a stationary distribution where the stationary probabilities for occupation of all but a finite number of states can be neglected [81].

In the following, we want to choose the transition matrix such that the stationary distribution becomes the distribution, $p[C_i]$, we are utilizing in our importance sampling [82]. Writing equation (2.89) out on component form and switching out $\pi_i$ with $p[C_i]$, we obtain

$$\sum_i p[C_i]\, \mathcal{P}_{ij} = p[C_j]. \tag{2.90}$$

We can now insert equation (2.86) to obtain the *balance equation*

$$\sum_i p[C_i]\, \mathcal{P}_{ij} = \sum_i p[C_j]\, \mathcal{P}_{ji}. \tag{2.91}$$

This is the condition that the transition probabilities need to satisfy in order for the limiting distribution to become $p[C_i]$. Although it is possible to base our Monte Carlo simulations on this equation [82], it is common to make the stricter demand that the equation should be satisfied term by term,

$$p[C_i]\,\mathcal{P}_{ij} = p[C_j]\,\mathcal{P}_{ji}. \tag{2.92}$$

This condition is called *detailed balance* and states that the probability that the system makes a transition from state $i$ to $j$ should be equal to the probability that the system makes the reverse transition [78].

To generate the configurations we need in our Monte Carlo simulations, we will choose an initial configuration for our system and then let the system perform a random walk in configuration space with transition probabilities that satisfy equation (2.92). After a sufficient number of steps, the system will, at least almost, be visiting configurations according to the probability distribution $p[C_i]$ and we can perform samples to determine the thermal average in equation (2.81) [78]. Equation (2.92) does, however, not fix the transition probabilities completely and we will, in the following, need to make some further choices.

### 2.4.4 Metropolis-Hastings Algorithm

A common way to determine transition probabilities that satisfy detailed balance is implemented in the *Metropolis-Hastings Algorithm* [83]. We split the transition probability $\mathcal{P}_{ij} \equiv \mathcal{P}(C_i \to C_j)$ into

$$\mathcal{P}(C_i \to C_j) = \mathcal{P}_P(C_i \to C_j)\,\mathcal{P}_A(C_i \to C_j), \tag{2.93}$$

where $\mathcal{P}_P(C_i \to C_j)$ is the probability of proposing the transition from configuration $i$ to $j$, and $\mathcal{P}_A(C_i \to C_j)$ is the probability of accepting the transition from configuration $i$ to $j$. The detailed balance condition then reads

$$p[C_i]\,\mathcal{P}_P(C_i \to C_j)\,\mathcal{P}_A(C_i \to C_j) = p[C_j]\,\mathcal{P}_P(C_j \to C_i)\,\mathcal{P}_A(C_j \to C_i). \tag{2.94}$$

It is clear that this condition can be satisfied by the following choice for the acceptance probability

$$\mathcal{P}_A(C_i \to C_j) = \min\left\{1,\ \frac{p[C_j]\,\mathcal{P}_P(C_j \to C_i)}{p[C_i]\,\mathcal{P}_P(C_i \to C_j)}\right\}. \tag{2.95}$$

The acceptance probability for the reverse process is obtained by exchange of the indices. Often, one will choose the selection probability to be equal in both directions, which leads to

$$\mathcal{P}_A(C_i \to C_j) = \min\left\{1,\ \frac{p[C_j]}{p[C_i]}\right\}. \tag{2.96}$$

If we now also plug in the expression for $p[C_i]$, we see that the unknown factor $Z$ cancels once again, producing

$$\mathcal{P}_A(C_i \to C_j) = \min\left\{1,\ e^{-\beta\left(H[C_j]-H[C_i]\right)}\right\}. \tag{2.97}$$

The thermal average in equation (2.81) can now be determined by the following algorithm:

1. Choose an initial configuration
2. Propose a new configuration
3. Calculate $\mathcal{P}_A$
4. Generate a random number $q \in [0, 1]$ from a uniform distribution
5. Accept the transition to the new configuration if $q \leq \mathcal{P}_A$, or, else, stay in the old configuration
6. If a sufficient number of steps have been performed, sample $O[C]$
7. Repeat until a satisfying number of samples have been obtained
8. Calculate $\langle O \rangle$

Configurations generated in this way will easily be correlated, which is a problem since our calculation of thermal averages rely on statistically independent samples. One normally therefore have to do several steps in the Markov chain in between measurements. The correlation between the configurations, measured in terms of Monte Carlo time (the number of steps in the Markov chain), can be quantified through the auto-correlation time [84], which will be introduced in the next section. Close to a critical point, this correlation time can diverge, preventing us from obtaining reliable results. This effect is called *critical slowing down*. The correlation between configurations depends on the update scheme we are utilizing in our Monte Carlo algorithm, i.e. how we propose new configurations [85]. The Metropolis-Hastings algorithm tells us the rate at which we should accept proposed transitions, but it does not specify how we should propose the needed configurations. We therefore have some freedom left to choose an update scheme that suits our specific system and purpose. For e.g. the Ising model consisting of spins on a lattice, a simple proposal scheme could be to repeatedly pick a random spin and attempt to flip it.

The goal of the Monte Carlo algorithm is to provide us with statistically independent configurations, according to the right probability distribution, as quickly as possible. In general, we therefore want to avoid making too many proposals that have a small chance of being accepted, so that we do not spend all our time in only a few configurations. At the same time, we might want to propose more drastic updates to decrease the correlation between configurations, meaning that fewer steps are necessary before we obtain a new independent configuration. Small updates that only change local quantities are referred to as local updates. A large number of such updates, working in the same direction, are necessary to change global quantities. Updates that can directly influence such global quantities are referred to as global updates. The flipping of a single spin in a spin system is an example of a local update, while, for the same system, an example of a global update could be to flip a large amount of spins at once, as implemented in cluster algorithms [86, 87].

In addition to taking many steps to produce a new configuration we can sample, an update scheme based solely on small iterative updates might cause our system to get stuck in some energetically favorable region of phase space and never manage to work its way through high-energy regions in order to reach other energetically favorable configurations. Global updates can alleviate this problem and potentially also combat critical slowing down [85]. The Monte Carlo algorithm we will focus on in this thesis, a so-called worm algorithm, incorporates, as we will see, such global updates.

The fact that it takes some time before the Markov chain generates configurations according to the correct distribution means that we will need a so-called *thermalization period* or *thermal equilibration period* before the we can start sampling. Ideally, the thermalization period would be infinitely long, but, in practice, this is obviously not possible. A reasonable point to start sampling can be established by continuously estimating values for relevant observables and waiting for the obtained values to converge.

### 2.4.5 Error Estimation

The procedure we have outlined is in principle exact as long as it is allowed to run forever. The errors in our estimates are therefore related to the fact that the simulations only run for a finite amount of time, both before and after we start sampling. The error related to the finite thermalization period can be difficult to establish, and one typically tries to include a thermalization period that is long enough for the error to be neglected altogether. Unfortunately this is not always possible, due to limited computational resources. After we have started sampling, the finite run-time means that our estimate will be based on a finite number of samples and that these samples will generally be somewhat correlated.

We start off by assuming that we can neglect the error due to the finite thermalization period and that we have found a way to generate statistically independent samples. The reminding error is then due to the fact that we are trying to calculate the average of a varying quantity $O$, using a finite number of samples. Since we are mimicking an ideal experimental determination of $\langle O \rangle$, the variation in $O$ should be equal to the variation one would experience from measurement to measurement in such an experiment, i.e. thermal fluctuations. Starting from the expression for $\langle O \rangle$ in equation (2.81), the estimated error takes the familiar form [85]

$$\xi_N = \sqrt{\frac{\langle O^2 \rangle_{\mathrm{MC}} - \langle O \rangle_{\mathrm{MC}}^2}{N-1}}, \tag{2.98}$$

If one were to be worried about the correctness of this expression because the configurations that go into the "mean calculation" in equation (2.81) are generated according to some complicated probability distribution, one can see that it follows straightforwardly from the results in the previous sections. Starting with the definition of the thermal average and taking into account that the result for $\langle O \rangle$ is obtained through importance sampling, we write the estimated error as

$$\xi_N = \frac{1}{Z} \frac{S_{f/p}}{\sqrt{N}}, \tag{2.99}$$

where $S_{f/p}$ is the "sample version" of equation (2.76), with $f$ identified with $Oe^{-\beta H}$ and $p$ identified with $e^{-\beta H}/Z$,

$$S_{f/p} = \sqrt{\frac{N}{N-1}} \sqrt{Z^2 \frac{1}{N} \sum_i \Big( O[C_i] \Big)^2 - Z^2 \Big( \frac{1}{N} \sum_i O[C_i] \Big)^2}. \tag{2.100}$$

Here, the configurations that go into the sums are generated according to $e^{-\beta H}/Z$. The result for $\xi_N$ then clearly reduces to equation (2.98). This is obviously also the error estimate we would use for an ideal experimental determination of the thermal average.

In the more realistic scenario where the configurations we generate are somewhat correlated, this effect can be taken into account by a modification of the error estimate [88]

$$\xi_N = \sqrt{(1 + 2\tau_A) \frac{\langle O^2 \rangle_{\mathrm{MC}} - \langle O \rangle_{\mathrm{MC}}^2}{N-1}}. \tag{2.101}$$

Here, $\tau_A$ is the previously mentioned auto-correlation time, which is the cut-off time for correlation between configurations in units of Monte Carlo time. The auto-correlation time is related to the auto-correlation function [84]

$$\phi_t \equiv \frac{1}{\langle O^2\rangle_{\mathrm{MC}} - \langle O\rangle^2_{\mathrm{MC}}}\left\{\frac{1}{N-t}\left(\sum_{i=1}^{N-t} O[C_i]\,O[C_{i+t}]\right) - \langle O\rangle^2_{\mathrm{MC}}\right\}, \tag{2.102}$$

which we often assume to have the following dependence on the auto-correlation time [84]

$$\phi_t \sim e^{-t/\tau_A}. \tag{2.103}$$

We can then estimate the auto-correlation time as

$$\tau_A \approx \sum_t \phi_t. \tag{2.104}$$

It is also possible to estimate the error $\xi_N$ using resampling methods such as *the bootstrap method* and *the jackknife method*. We will focus on the bootstrap method. To perform bootstrapping, we will need to have kept track of the $N$ samples of $O_i$ that were produced during the simulation. We store these values in a list of length $N$. We then choose $N$ random samples from the list without removing samples that have already been chosen, meaning that the same sample could be picked out several times. We then use these N chosen samples to calculate an average value $\overline{O}^{(1)}$. We repeat this procedure $m$ times, picking out $N$ samples from the list and calculating a new average value $\overline{O}^{(i)}$ each time. We can then use these values to calculate new averages

$$\begin{aligned}\overline{\overline{O}} &= \frac{1}{m}\sum_{i=1}^{m}\overline{O}^{(i)},\\ \overline{\overline{O^2}} &= \frac{1}{m}\sum_{i=1}^{m}\left(\overline{O}^{(i)}\right)^2.\end{aligned} \tag{2.105}$$

It can then be shown that the bootstrap standard deviation

$$S = \sqrt{\frac{\sum_{i=1}^{m}\left(\overline{O}^{(i)} - \overline{\overline{O}}\right)}{m-1}} = \sqrt{\frac{m}{m-1}}\sqrt{\overline{\overline{O^2}} - \overline{\overline{O}}^2}, \tag{2.106}$$

is an estimate of the error $\xi_N$ [89]. A intuitive argument for why there is not an extra factor $1/\sqrt{m}$ in this expression is that it would imply that we could reduce the error by performing more resamplings. Often, one will need to perform an initial blocking of the values $O_i$, to properly address the correlation between the measurements. One then reduces the list of $N$ samples $O_i$ to a list of $N/M$ values $O_i^*$, where each $O_i^*$ is the average of $M$ consecutive $O_i$'s. One should make sure to include enough samples in each block to make sure that the resulting values $O_i^*$ are statistically independent of each other.

In addition to the finite thermalization period, the pseudorandom number generator we use in the simulations (e.g. to decide whether to accept a new configuration or not) can produce errors that are not included in the error estimate $\xi_N$. The Mersenne Twister algorithm [90] for pseudorandom number generation has been used in all simulations presented in chapter 3.

## 2.5 Path Integral Formulation for the Bose-Hubbard Model

We have now outlined a method for calculating thermal averages for a classical system. Unfortunately, our system of interest, described by the Bose-Hubbard model, is a quantum system. It is, however, possible to map our quantum system onto a $(d+1)$-dimensional system described by a set of classical configurations [35]. This can be achieved by formulating the problem in terms of Feynman's path integral formalism.

### 2.5.1 Derivation

We start by splitting the Hamiltonian in equation (2.24) into the diagonal and off-diagonal part with respect to the lattice site occupation number basis $\{|n_i\rangle\}$, $H \equiv H_0 + V$,

$$H_0 \equiv \frac{1}{2}\sum_{i\sigma\sigma'} U_{\sigma\sigma'} n_{i\sigma}(n_{i\sigma'} - \delta_{\sigma\sigma'}) - \sum_{i\sigma} \mu_\sigma n_{i\sigma}, \tag{2.107}$$

$$V \equiv -t \sum_{\langle ij\rangle\sigma} a^\dagger_{i\sigma} a_{j\sigma}. \tag{2.108}$$

It should be noted that the Hamiltonian includes a term on the form $-\mu N$, meaning that we have performed the redefinition $H - \mu N \to H$, and that we are working in the grand canonical ensemble where the time evolution is governed by this redefined operator. We then perform a Wick rotation $t \to -i\tau$, transforming the time, $t$, (not the hopping amplitude in the above equation) into an imaginary variable by a $\pi/2$-rotation in the complex plane [91]. The variable $\tau$ is real, but it is often referred to as *imaginary time*, because the inverse Wick rotation transforms $\tau \to it$, where $t$ now is real. In the interaction picture, considering $V$ as the "perturbing" part of the Hamiltonian, we can then write the equation of motion for the time evolution operator as [92]

$$\frac{\partial}{\partial\tau} U_I(\tau) = -V_I(\tau) U_I(\tau). \tag{2.109}$$

Integrating from 0 to $\beta$ produces

$$U_I(\beta) = 1 - \int_0^\beta \mathrm{d}\tau_1 V_I(\tau_1) U_I(\tau_1), \tag{2.110}$$

where the expression on the right side can be repeatedly inserted into itself to produce the perturbation series

$$U_I(\beta) = 1 - \int_0^\beta \mathrm{d}\tau_1 V_I(\tau_1) + \sum_{m=2}^{\infty} (-1)^m \int_0^\beta \mathrm{d}\tau_m \int_0^{\tau_m} \mathrm{d}\tau_{m-1} \ldots \int_0^{\tau_2} \mathrm{d}\tau_1 V_I(\tau_m) \ldots V_I(\tau_1). \tag{2.111}$$

Since the Hamiltonian in question is not explicitly time-dependent, the evolution operator in the interaction picture, rewritten in terms of imaginary time, becomes simply

$$U_I(\tau) = e^{H_0\tau} e^{-H\tau}, \tag{2.112}$$

corresponding to evolving the states under the perturbing part of the Hamiltonian by first evolving forward under the total Hamiltonian and then backward under the unperturbed Hamiltonian. Starting from the expression for the partition function

$$Z = \mathrm{Tr}\left\{e^{-\beta H}\right\}, \tag{2.113}$$

where $\beta = \frac{1}{T}$, we can rewrite this as

$$Z = \mathrm{Tr}\left\{e^{-\beta H_0} U_I(\beta)\right\}. \tag{2.114}$$

Performing the trace in the eigenbasis of $H_0$, the partition function takes the form

$$Z = \sum_\alpha e^{-\beta E_\alpha} \langle\alpha| \left(1 - \int_0^\beta \mathrm{d}\tau_1 V_I(\tau_1) + \sum_{m=2}^{\infty} (-1)^m \int_0^\beta \mathrm{d}\tau_m \int_0^{\tau_m} \mathrm{d}\tau_{m-1} \ldots \int_0^{\tau_2} \mathrm{d}\tau_1 V_I(\tau_m) \ldots V_I(\tau_1)\right) |\alpha\rangle \,. \tag{2.115}$$

Inserting resolutions of the identity, writing out the operators in the Schrödinger picture,

$$V_I(\tau_i) = e^{H_0 \tau_i} \, V \, e^{-H_0 \tau_i}, \tag{2.116}$$

and defining

$$\langle\alpha_k| \, V \, |\alpha_{k-1}\rangle \equiv V_{\alpha_k, \alpha_{k-1}}, \tag{2.117}$$

the expression can be further rewritten as

$$\begin{aligned} Z = \sum_\alpha e^{-\beta E_\alpha} \Bigg[1 - \int_0^\beta \mathrm{d}\tau \, V_{\alpha,\alpha} + \sum_{m=2}^{\infty} (-1)^m \int_0^\beta \mathrm{d}\tau_m \int_0^{\tau_m} \mathrm{d}\tau_{m-1} \ldots \int_0^{\tau_2} \mathrm{d}\tau_1 \sum_{\alpha_1, \ldots, \alpha_{m-1}} \\ \times \left(e^{\tau_m E_\alpha} V_{\alpha, \alpha_{m-1}} e^{-\tau_m E_{\alpha_{m-1}}}\right) \left(e^{\tau_{m-1} E_{\alpha_{m-1}}} V_{\alpha_{m-1}, \alpha_{m-2}} e^{-\tau_{m-1} E_{\alpha_{m-2}}}\right) \ldots \left(e^{\tau_1 E_{\alpha_1}} V_{\alpha_1, \alpha} e^{-\tau_1 E_\alpha}\right)\Bigg]. \end{aligned} \tag{2.118}$$

We now identify a configuration $C$ with a set of parameters $\{m, \tau_1, \ldots, \tau_m, \alpha, \alpha_1, \ldots \alpha_{m-1}\}$, where $0 < \tau_1 < \tau_2 < \ldots < \tau_m < \beta$, corresponding to a term in the above expansion. The partition function can then be expressed as

$$Z = \sum_C W[C], \tag{2.119}$$

and average values can be computed as

$$\langle O \rangle = \frac{1}{Z} \sum_C O[C] \, W[C], \tag{2.120}$$

for some observable $O$ that is diagonal in the eigenbasis of the unperturbed Hamiltonian. For a general term in this series, there are clearly $m$ factors $V_{\alpha\beta}$ that each introduce a minus sign, which cancel with the prefactor $(-1)^m$. All terms are therefore positive, meaning that we can identify the normalized weighting function $W(C)/Z$ with the probability of finding the system in the given configuration. Following the method that we have outlined, we then perform importance sampling according to the distribution $W(C)/Z$. The thermal average can now, once again, be computed as

$$\langle O \rangle_{\mathrm{MC}} = \frac{1}{N} \sum_{i=1}^{N} O[C_i]. \tag{2.121}$$

A configuration, $C$, can be visualized by a worldlines diagram, as shown in figure 2.3. Particles of different components can easily be incorporated in such a diagram, but for simplicity we stick to the one-component case. Here, a dotted line corresponds to having no particles at a lattice point at a given time, a solid line corresponds to a single particle and a double line corresponds to two particles. A solid line therefore represents the imaginary time trajectory of a particle. For a given time, the arrangement of particles on the different lattice sites defines a state $\alpha_i$. A single black dot, marking a 90° angle in a solid line, will be referred to as a *kink* and the set of two corresponding kinks that take place at the same time will be referred to as a *kink pair*. A kink pair corresponds to a particle hopping from one site to a neighboring site; an action that will often be referred to as a jump. For each time $\tau_i$ in $\{m, \tau_1, \ldots, \tau_m, \alpha, \alpha_1, \ldots \alpha_{m-1}\}$ a jump takes place, where the state before and after the jump are determined by the states $\alpha_{i-1}$ and $\alpha_i$. The system starts in the state $\alpha$, then at time $\tau_1$ the system changes state to $\alpha_1$ and so on. Finally at the time $\tau_m$ the system returns to its initial state, as determined by the expression in equation (2.118). The number $m$ clearly corresponds to the number of kink pairs in the worldlines diagram.

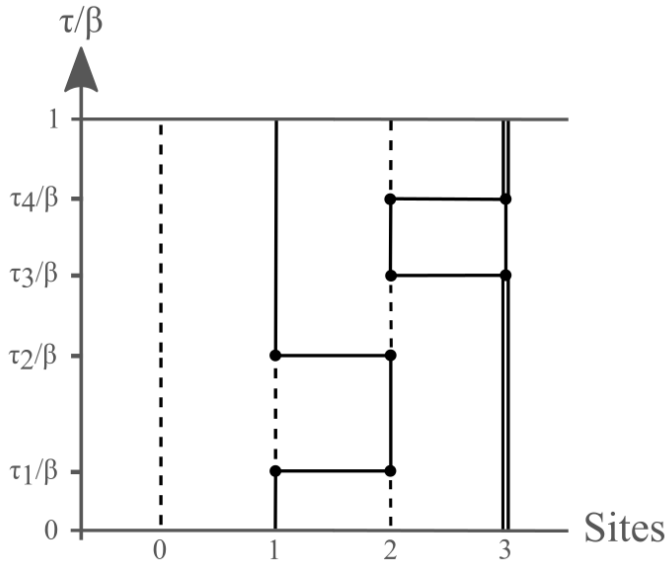


Figure 2.3: Worldlines diagram, visualizing a configuration with $m = 4$ for a one-dimensional system with four lattice sites and only one type of particle.

### 2.5.2 Example Configuration

The worldlines diagram in figure 2.3 corresponds to a configuration $\{m = 4, \tau_1, \tau_2, \tau_3, \tau_4, \alpha, \alpha_1, \alpha_2, \alpha_3\}$. Since our example considers the one-component case, we once again introduce the one-component Bose-Hubbard model from equation (2.30)

$$H_0 = \frac{U}{2}\sum_i n_i(n_i-1) - \mu\sum_i n_i, \tag{2.122}$$

$$V = -t\sum_{\langle ij\rangle} a_i^\dagger a_j. \tag{2.123}$$

For the configuration in the figure, the weight $W(C)$ becomes

$$\begin{aligned} W(C) = e^{-\beta E_\alpha}(-1)^4 &\left(e^{\tau_4 E_\alpha} V_{\alpha,\alpha_3} e^{-\tau_4 E_{\alpha_3}}\right)\left(e^{\tau_3 E_{\alpha_3}} V_{\alpha_3,\alpha_2} e^{-\tau_3 E_{\alpha_2}}\right) \\ &\times \left(e^{\tau_2 E_{\alpha_2}} V_{\alpha_2,\alpha_1} e^{-\tau_2 E_{\alpha_1}}\right)\left(e^{\tau_1 E_{\alpha_1}} V_{\alpha_1,\alpha} e^{-\tau_1 E_\alpha}\right). \end{aligned} \tag{2.124}$$

Writing the states on the form $|n_1, n_2, n_3, n_4\rangle$, and setting $\mu = 0$, $U = 1$ and $t = 1$ we have

$$\begin{aligned} |\,\alpha\,\rangle &= |0,1,0,2\rangle\,, & E_\alpha &= 1 \\ |\alpha_1\rangle &= |0,0,1,2\rangle\,, & E_{\alpha_1} &= 1 \\ |\alpha_2\rangle &= |0,1,0,2\rangle\,, & E_{\alpha_2} &= 1 \\ |\alpha_3\rangle &= |0,1,1,1\rangle\,, & E_{\alpha_3} &= 0, \end{aligned}$$

and the contributions from the hopping term takes the form

$$V_{\alpha_k,\alpha_{k-1}} = \langle\alpha_k|\left(-t\sum_{\langle ij\rangle} a_i^\dagger a_j\right)|\alpha_{k-1}\rangle = -t\sqrt{n_i^{\alpha_{k-1}}+1}\sqrt{n_j^{\alpha_{k-1}}} \tag{2.125}$$

where $n_j^{\alpha_{k-1}}$ is the number of particle in the state $\alpha_{k-1}$, on the site where a particle is annihilated when transitioning from the state $\alpha_{k-1}$ to the state $\alpha_k$. Likewise, $n_i^{\alpha_{k-1}}$ is the number of particles in the state $\alpha_{k-1}$, on the site where a new particle is created when transitioning from the state $\alpha_{k-1}$ to the state $\alpha_k$. The specific contributions in our example then become

$$\begin{aligned} V_{\alpha_1,\alpha} &= -1 \\ V_{\alpha_2,\alpha_1} &= -1 \\ V_{\alpha_3,\alpha_2} &= -\sqrt{2} \\ V_{\alpha,\alpha_3} &= -\sqrt{2}. \end{aligned}$$

### 2.5.3 Winding Numbers and Superfluid Density

Due to the periodicity in the spatial dimensions, it is also possible for the worldlines to wind across a spatial periodic boundary, as illustrated in figure 2.4. In the one-component case, the statistics of the worldlines are related to the superfluid density through the Pollock-Ceperley formula [93]

$$\rho = \frac{m^2 L^{2-d}}{d\beta}\langle W^2\rangle, \tag{2.126}$$

where $\vec{W}$ is the $d$-dimensional winding number vector where each component of the vector counts the net number of times the worldlines wind across the periodic boundary in the corresponding spatial

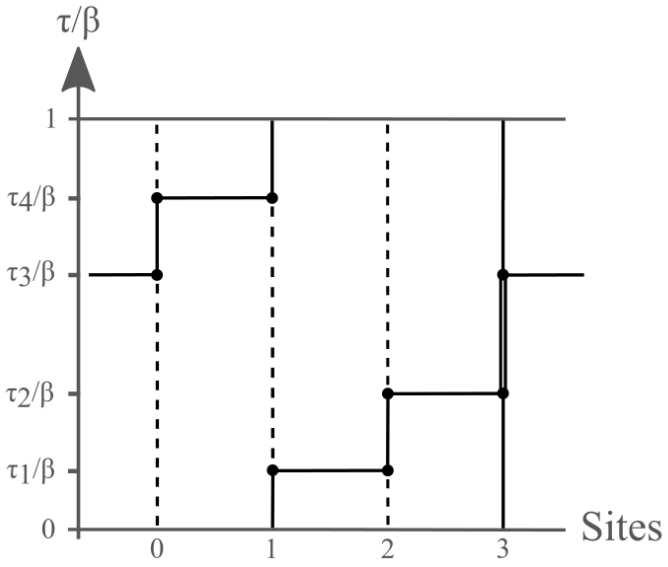


Figure 2.4: Worldlines diagram showing winding across a periodic boundary.

direction. Following the derivation in [47], we will shortly see that the superfluid densities of the multicomponent system is given by

$$\rho_{\alpha\nu} = \frac{m_\alpha m_\nu L^{2-d}}{d\beta} \langle \vec{W}_\alpha \cdot \vec{W}_\nu \rangle, \tag{2.127}$$

where $\vec{W}_\alpha$ is the winding number vector corresponding to worldlines representing trajectories of particles of type $\alpha$. The winding number vectors are computed straightforwardly from the configurations that are generated in the Monte Carlo simulations and the averages are obtained to determine the diagonal superfluid densities, as well as the off-diagonal superfluid drag densities.

There exists more than one definition of "superfluid density" and in dimensions less than 3, these are generally not equivalent [35, 94]. The superfluid density we have defined in our expression for the free energy is given by the system's statistical response to a static gauge field and is simply proportional to the second derivative of the free energy with respect to an infinitesimal phase twist [43]. We will therefore examine the response of the system to infinitesimal phase twists in order to obtain an expression for the drag, as foreshadowed in section 2.3.3, where we noted that a the introduction of a gauge field, $\vec{A} = -\vec{\chi}/L$, corresponding to setting the superfluid in motion with velocity $\vec{v} = \gamma\vec{\chi}/L$, introduced a phase factor $e^{i\vec{\chi}\cdot\vec{\mu}}$. Here $\vec{\mu}$ denotes a spatial unit vector. Similarly, the twisted boundary conditions introduce a phase factor of the same form for each time a worldline crosses a spatial periodic boundary [35]. This follows from the Peierls substitution [95], which includes a gauge field in a lattice problem by adding a phase factor to the hopping amplitude. Attempting to gauge away the field in the usual way results in a phase factor associated with all hopping processes that cross a spatial periodic boundary. The partition function with infinitesimal phase twists can then be expressed as

$$Z_{\vec{\chi}_a,\vec{\chi}_b,\vec{\chi}_c\neq 0} = \sum_{\vec{W}_a,\vec{W}_b,\vec{W}_a} e^{i(\vec{\chi}_a\cdot\vec{W}_a+\vec{\chi}_b\cdot\vec{W}_b+\vec{\chi}_c\cdot\vec{W}_c)}\, Z_{\vec{W}_a,\vec{W}_b,\vec{W}_c}, \tag{2.128}$$

where $Z_{\vec{W}_a,\vec{W}_b,\vec{W}_c}$ is the contributions to the partition function from configurations with fixed winding numbers. The partition function without the phase twists is similarly expressed as

$$Z_{\vec{\chi}_a,\vec{\chi}_b,\vec{\chi}_c=0} = \sum_{\vec{W}_a,\vec{W}_b,\vec{W}_a} Z_{\vec{W}_a,\vec{W}_b,\vec{W}_c}. \tag{2.129}$$

Defining

$$F_s = F_{\vec{\chi}_a,\vec{\chi}_b,\vec{\chi}_c\neq 0} - F_{\vec{\chi}_a,\vec{\chi}_b,\vec{\chi}_c=0} \tag{2.130}$$

as the free-energy difference associated with the introduction of the phase twists, we get

$$\begin{aligned} e^{-\beta F_s} &= \frac{e^{-\beta F_{\vec{\chi}_a,\vec{\chi}_b,\vec{\chi}_c\neq 0}}}{e^{-\beta F_{\vec{\chi}_a,\vec{\chi}_b,\vec{\chi}_c=0}}} = \frac{Z_{\vec{\chi}_a,\vec{\chi}_b,\vec{\chi}_c\neq 0}}{Z_{\vec{\chi}_a,\vec{\chi}_b,\vec{\chi}_c=0}} = \frac{\sum_{\vec{W}_a,\vec{W}_b,\vec{W}_c} e^{i(\vec{\chi}_a\cdot\vec{W}_a+\vec{\chi}_b\cdot\vec{W}_b+\vec{\chi}_c\cdot\vec{W}_c)}\, Z_{\vec{W}_a,\vec{W}_b,\vec{W}_c}}{\sum_{\vec{W}_a,\vec{W}_b,\vec{W}_c} Z_{\vec{W}_a,\vec{W}_b,\vec{W}_c}} \\ &= \Big\langle e^{i(\vec{\chi}_a\cdot\vec{W}_a+\vec{\chi}_b\cdot\vec{W}_b+\vec{\chi}_c\cdot\vec{W}_c)} \Big\rangle. \end{aligned} \tag{2.131}$$

As we assume infinitesimal phase twists, we naturally expand the right-hand side in small phase twists. The worldlines corresponding to different particle types will typically have a preference for winding in the same or opposite direction as each other, but whether the winding takes place in the positive or negative spatial direction is completely arbitrary. We will therefore always have $\langle \vec{W}_\alpha \rangle = 0$. Moreover, as we are interested in an an isotropic geometry, i.e. a $d$-dimensional cubic lattice with equal system length in all directions, the different components of the winding number vector, corresponding to different spatial directions, will be uncorrelated and there is no preference for winding in any specific spatial direction. Defining the right-hand side of equation (2.131) as $\langle e^{iq} \rangle$, we can express it as

$$\langle e^{iq} \rangle = \langle 1 + iq + \frac{1}{2}(iq)^2 + \dots \rangle \approx 1 - \frac{1}{2}\langle q^2 \rangle. \tag{2.132}$$

Expanding also the left-hand side of equation (2.131) to lowest non-trivial order, we then obtain,

$$\begin{aligned} \beta F_s = \frac{1}{2}\Big\langle &(\vec{\chi}_a\cdot\vec{W}_a)^2 + (\vec{\chi}_b\cdot\vec{W}_b)^2 + (\vec{\chi}_c\cdot\vec{W}_c)^2 + 2(\vec{\chi}_a\cdot\vec{W}_a)(\vec{\chi}_b\cdot\vec{W}_b) \\ &+ 2(\vec{\chi}_a\cdot\vec{W}_a)(\vec{\chi}_c\cdot\vec{W}_c) + 2(\vec{\chi}_b\cdot\vec{W}_b)(\vec{\chi}_c\cdot\vec{W}_c)\Big\rangle. \end{aligned} \tag{2.133}$$

Expressing vector components through superscripts and using Einstein summation convention we can write

$$\big\langle (\vec{\chi}_\alpha\cdot\vec{W}_\alpha)(\vec{\chi}_\nu\cdot\vec{W}_\nu)\big\rangle = \big\langle \chi_\alpha^{(i)} W_\alpha^{(i)} \chi_\nu^{(j)} W_\nu^{(j)} \big\rangle = \chi_\alpha^{(i)}\chi_\nu^{(j)} \frac{\delta_{ij}\langle \vec{W}_\alpha\cdot\vec{W}_\nu\rangle}{d} = \frac{\langle \vec{W}_\alpha\cdot\vec{W}_\nu\rangle \vec{\chi}_\alpha\cdot\vec{\chi}_\nu}{d}. \tag{2.134}$$

We insert this into the expression for the the free energy associated with the introduction of the phase twists in equation (2.133) and express the phase twists in terms of $\vec{v}_\alpha$

$$\vec{\chi}_\alpha = m_\alpha \vec{v}_\alpha L. \tag{2.135}$$

Making the connection to identify $F_s$ with the free energy associated with the phase-twist induced superfluid motion of the system, we obtain the final expression for the free energy density of the superfluid part of the system

$$f_s = \frac{L^{2-d}}{\beta d}\Bigg(\frac{1}{2}m_a^2\langle W_a^2\rangle v_a^2 + \frac{1}{2}m_b^2\langle W_b^2\rangle v_b^2 + \frac{1}{2}m_c^2\langle W_c^2\rangle v_c^2 + m_a m_b\langle \vec{W}_a\cdot\vec{W}_b\rangle \vec{v}_a\cdot\vec{v}_b \\ + m_a m_c\langle \vec{W}_a\cdot\vec{W}_c\rangle \vec{v}_a\cdot\vec{v}_c + m_b m_c\langle \vec{W}_b\cdot\vec{W}_c\rangle \vec{v}_b\cdot\vec{v}_c\Bigg). \tag{2.136}$$

Comparison with equation (2.65) then produces equation (2.127). Finally, we introduce a useful quantity [47]

$$\varrho_{\alpha\nu} \equiv \frac{\rho_{\alpha\nu}}{\sqrt{\rho_{\alpha\alpha}\rho_{\nu\nu}}} = \frac{\langle \vec{W}_\alpha\cdot\vec{W}_\nu\rangle}{\sqrt{\langle W_\alpha^2\rangle\langle W_\nu^2\rangle}}, \tag{2.137}$$

which we will refer to as the normalized drag.

From the formula in equation (2.127), relating the winding of worldlines to superfluid densities, we see that non-zero superfluid drag densities arise from worldlines, corresponding to different components, winding in the same or opposite direction. Examples of multicomponent configurations that contribute to positive and negative drag, respectively, are shown in figure 2.5. The motivation behind the winding is to avoid paying on-site interaction energy by separating the particles.

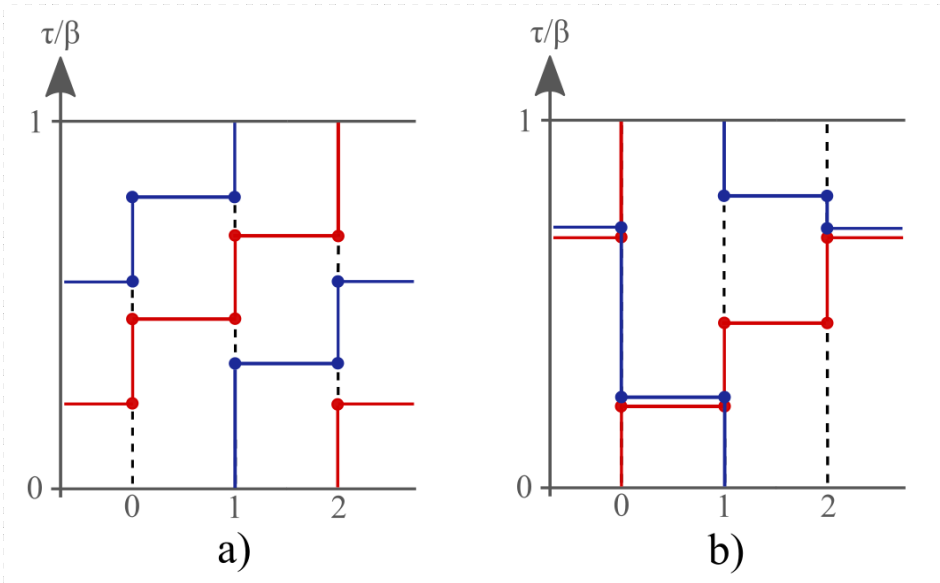


Figure 2.5: Examples of configurations that contribute to a positive, a), and negative, b), superfluid drag between two superfluid components. Worldlines corresponding to different components have different colors.

## 2.6 Worm Algorithm

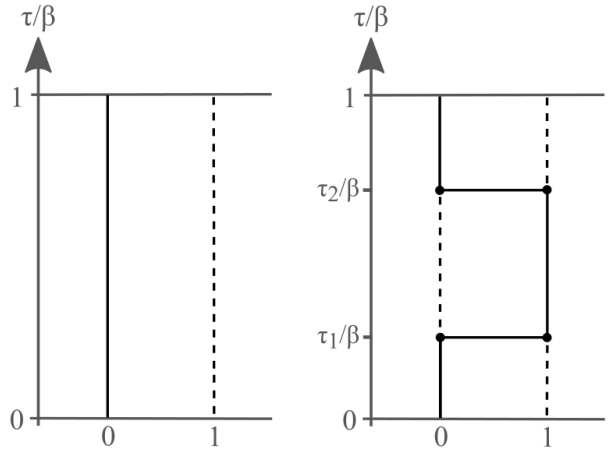


Figure 2.6: Insertion of a pair of jumps.

The reminding question is how we will generate configurations of the form introduced in the previous section. One option could be to allow for updates where we insert a pair of jumps, as shown in figure 2.6, change the time of an existing jump or insert/delete a particle on a lattice site [96]. Using these updates we could produce many of the possible configurations, but it would e.g. not be possible to create a configuration with a different winding number than the one we started with, destroying the ergodicity of our update scheme. A solution to this problem was proposed by Prokof'ev and Svistunov through the *worm algorithm* [97, 98]. An updated version of this algorithm, proposed by Pollet et al., is often referred to as the *directed worm algorithm* [99]. We will focus on the version of the directed worm algorithm outlined by P. N. Ma [96]. These algorithms are able to sample the configuration space ergodically and are generally resistant to critical slowing-down [97]. Although it will not be useful for our purposes, they are also well-equipped for calculation of e.g. the Matsubara Green's function [100],

$$G(\nu, \tau; \nu'\tau') = -\langle\, \mathcal{T}_\tau \left[ a_\nu(\tau) a^\dagger_{\nu'}(\tau') \right] \rangle. \tag{2.138}$$

Here $\mathcal{T}_\tau$ is the time-ordering operator.

The basic concept of the algorithm is that we insert two discontinuities into the worldlines diagram, where either a particle is created or annihilated, as illustrated in figure 2.7 a). These discontinuities are referred to as the head and the tail of a worm. The tail is fixed in space-time, while the head is free to move around. A configuration with two such discontinuities, where the particle number is not conserved, belongs to an extended configuration space and contributes to the calculation of the Matsubara Green's function [100]. For our purposes, such configurations are not valid configurations that we should include in our Monte Carlo estimate of the average of some diagonal variable. However, at some point, the head will encounter the tail and remove the worm altogether. The reminding configuration is then a valid configuration that we can sample. This process is shown in figure 2.7 b-c).

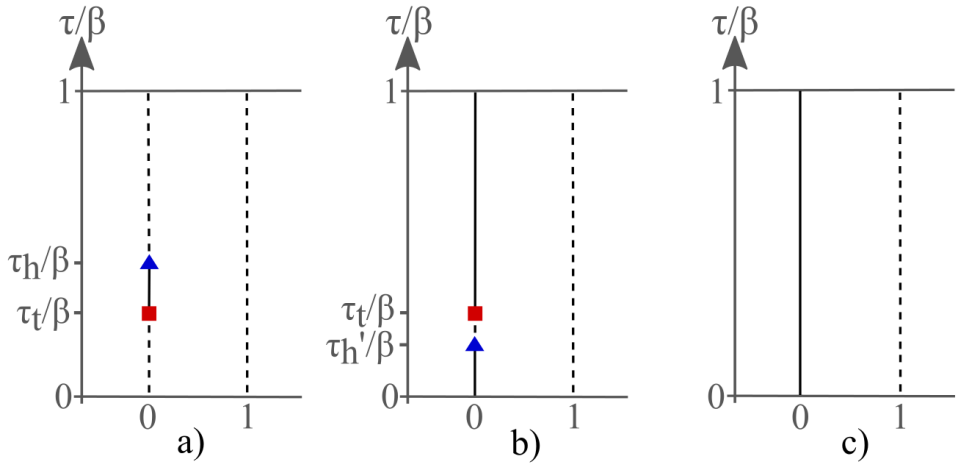


Figure 2.7: Worldlines diagram with an inserted worm, consisting of a head (blue triangle) and a tail (red square). The head propagates until it reaches the tail and removes the worm altogether.

Instead of just moving in a straight line, the head of the worm can, as we will see, turn around or perform hops to neighboring sites and across spatial periodic boundaries, producing all possible configurations. The head can propagate both forward and backward in imaginary time and the wormhead operator can be either a creation or annihilation operator. To return to the initial empty configuration preceding the configuration in 2.7 a), we could e.g. insert into c) a worm propagating froward in time where the head operator is a creation operator (and the tail operator therefore is an annihilation operator), or another worm where the head is an annihilation operator, but where the head this time propagates backwards in time. The examples that follow will mostly concern the case where the wormhead operator is an annihilation operator, but examples of processes where the wormhead operator is a creation operator are given by time-reversal. This can be seen by flipping the worldlines diagrams upside-down, reversing the time and wormhead direction and viewing transitions between configurations in the opposite direction. The transition from a) to b) then transforms into a process where a wormhead acting as a creation operator moves forward in time, crosses the periodic boundary in the time-direction and approaches the tail.

The weighting function for the extended configurations takes the form

$$\begin{aligned} W_{\text{ext}}(C) = e^{-\beta E_\alpha}(-1)^m \left(e^{\tau_m E_\alpha} V_{\alpha,\alpha_{m-1}} e^{-\tau_m E_{\alpha_{m-1}}}\right) \dots \left(e^{\tau_p E_{\alpha_p}} \langle \alpha_p | \, a_p^\dagger \, | \alpha_{p-1} \rangle \, e^{-\tau_p E_{\alpha_{p-1}}}\right) \dots \\ \times \left(e^{\tau_q E_{\alpha_q}} \langle \alpha_q | \, a_q \, | \alpha_{q-1} \rangle \, e^{-\tau_q E_{\alpha_{q-1}}}\right) \dots \left(e^{\tau_1 E_{\alpha_1}} V_{\alpha_1,\alpha} e^{-\tau_1 E_\alpha}\right). \end{aligned} \tag{2.139}$$

Here $a_p^\dagger$ should be understood as the creation operator that is necessary to bring the system from the state $\alpha_{p-1}$ to the state $\alpha_p$, and similarly for $a_q$. The placement of these factors in the weighting function is determined by their corresponding times and their relative order is not fixed in the way displayed in equation (2.139).

To outline the algorithm we use an instructive example, heavily inspired by [96], illustrated in figure 2.8. We consider the time at the beginning and the end of this process to be fixed. The process should then be balanced with the reverse move, shown in figure 2.9. We will not demand that each step in these processes satisfy detailed balance because the requirement that the combined moves are detailed balanced will be sufficient to make sure that the resulting transitions between valid configurations are

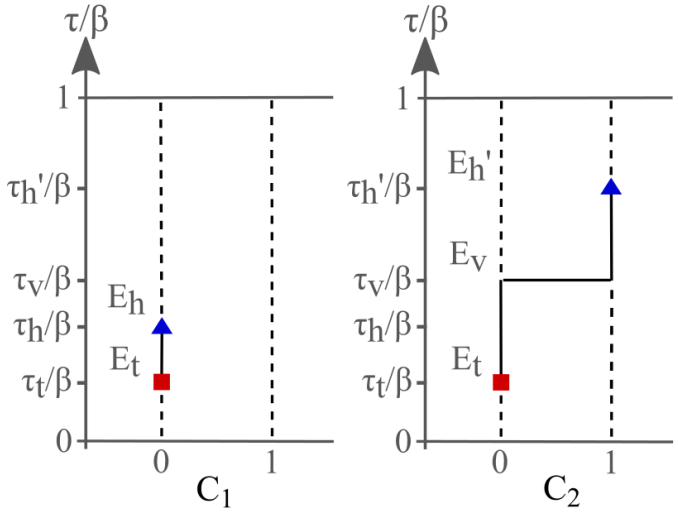


Figure 2.8: Illustration of the transition from an extended configuration $C_1$ to another extended configuration $C_2$.

detailed balanced [96]. Free propagation of the wormhead will be referred to as unhalted movement, while propagation that ends because the wormhead encounters an obstacle, such as a kink, will be referred to as halted movement. The forward process in figure 2.8 can then be divided into the following steps:

1. Unhalted movement from $\tau_h$ to $\tau_v$
2. Hop from site 0 to site 1
3. Halted movement from $\tau_v^+$ to $\tau_{h'}$,

while the reverse move in figure 2.9 can be broken up into:

1. Halted movement from $\tau_{h'}$ to $\tau_v$
2. Hop from site 1 to site 0
3. Halted movement from $\tau_v^-$ to $\tau_h$.

The direction of the wormhead is simply an artifact of our algorithm and is not an inherent quality of the configurations. We can therefore identify the first configuration in figure 2.8 and the second configuration in figure 2.9 with the label $C_1$, and the reminding two configurations with the label $C_2$. Using the expression for the weighting function in equation (2.139) and comparing the two configurations, we can write

$$\frac{W_{\text{ext}}(C_2)}{W_{\text{ext}}(C_1)} = \frac{\left(e^{\tau_{h'}E_{h'}}\,\langle\alpha_{h'}|\,a_1\,|\alpha_v\rangle\,e^{-\tau_{h'}E_v}\right)\left(e^{\tau_v E_v}t\,\langle\alpha_v|\,a_1^\dagger a_0\,|\alpha_t\rangle\,e^{-\tau_v E_t}\right)}{\left(e^{\tau_h E_h}\,\langle\alpha_h|\,a_0\,|\alpha_t\rangle\,e^{-\tau_h E_t}\right)}. \tag{2.140}$$

In addition to the index indicating the site on which a particle is created or annihilated the creation/annihilation operators should, in the multicomponent case, also have an index showing the

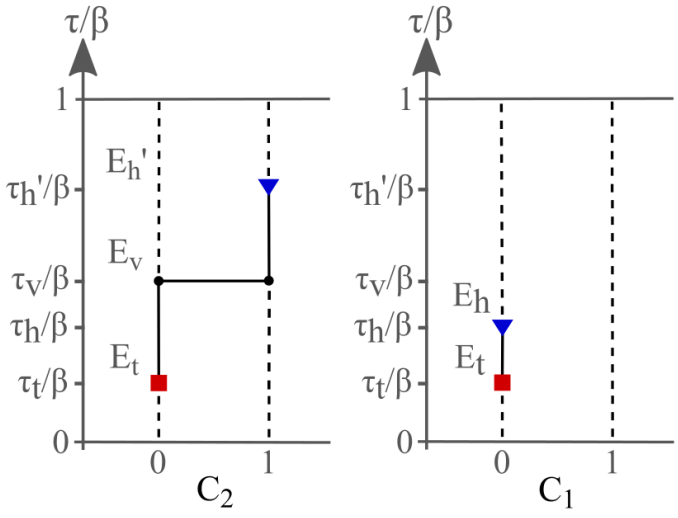


Figure 2.9: The reverse of the process in figure 2.8, illustrating the transition from an extended configuration $C_2$ to another extended configuration $C_1$.

component of the particle that is created/annihilated. For the most part, we will focus on the one-component case and just comment on the few differences that arise in the multicomponent case as we go along. We see that all the factors that contribute to the above expression are related to the propagating worm, which belongs to a component, and all the relevant operators will therefore correspond to the same component. Any present particles of different components will simply contribute to the energies $E$.

The reminding indices follow the usual convention where the state with a given index is the state right after the time with the same index. In the case where the same time is followed by different states in the two different configurations, it is the configuration where an action takes place at this time that defines the state with the corresponding index. The energy $E_h$ is therefore defined by configuration $C_1$, while $E_{h'}$ is defined by configuration $C_2$. Using that these two energies are equal, rewriting the fraction on the right-hand side of (2.140) and plugging in equation (2.94) on the left-hand side, we can write

$$\frac{\mathcal{P}_P(C_1 \to C_2)\,\mathcal{P}_A(C_1 \to C_2)}{\mathcal{P}_P(C_2 \to C_1)\,\mathcal{P}_A(C_2 \to C_1)} = \left(\frac{e^{-E_v(\tau_{h'}-\tau_v)}\,E_t e^{-E_t(\tau_v-\tau_h)}}{e^{-E_{h'}(\tau_{h'}-\tau_v)}e^{-E_{h'}(\tau_v-\tau_h)}}\right)\left(\frac{t\,\langle\alpha_{h'}|\,a_1\,|\alpha_v\rangle\,\langle\alpha_v|\,a_1^\dagger a_0\,|\alpha_t\rangle}{E_t\,\langle\alpha_h|\,a_0\,|\alpha_t\rangle}\right). \tag{2.141}$$

We now want the proposal probabilities to take care of the first parenthesis on the right-hand side, allowing us to determine the acceptance probabilities by the condition specified by the Metropolis-Hastings algorithm

$$\mathcal{P}_A(C_1 \to C_2) = \min\left\{1,\ \frac{t\,\langle\alpha_{h'}|\,a_1\,|\alpha_v\rangle\,\langle\alpha_v|\,a_1^\dagger a_0\,|\alpha_t\rangle}{E_t\,\langle\alpha_h|\,a_0\,|\alpha_t\rangle}\right\}. \tag{2.142}$$

This expression is easy to compute and does not require us to calculate the weight of the entire configurations. It can also be simplified by noticing that the contribution from the wormhead operator

in configuration $C_1$ will always be cancelled out by the contribution from the kink that is inserted on the same site. The reminding other kink in the kink pair and the wormhead contribution in configuration $C_2$, simply acts with the operator $a_1 a_1^\dagger$, which is a commutation relation away from measuring the number of particles (of the same component as the worm operators) at site 1 right before the inserted kink pair. The acceptance probability can therefore be expressed as

$$\mathcal{P}_A(C_1 \to C_2) = \min\left\{1,\ \frac{t\,\langle\alpha_t|\,(n_1+1)\,|\alpha_t\rangle}{E_t}\right\}. \tag{2.143}$$

The acceptance probability for the reverse process is just given by exchanging the nominator and denominator in the expression on the right-hand side.

Now, we just need to take care of the proposal probabilities. We define $\tau_{ab} \equiv \tau_a - \tau_b$ and associate the unhalted movement from $\tau_h$ to $\tau_v$ with the factor

$$E_t e^{-E_t \tau_{vh}}. \tag{2.144}$$

We take this as the probability of proposing the move and accept it with probability 1. The time-shifts are therefore distributed according to the exponential distribution

$$f(t, E) = E e^{-Et}, \quad t \geq 0, \tag{2.145}$$

which is a normalized probability distribution, describing the time between events in a Poisson point process [101]. The probability of proposing the halted movement from $\tau_v^+$ to $\tau_{h'}$ should be given by

$$\int_{\tau_{h'v}}^{\infty} \mathrm{d}\tau_{sv}\, E_v e^{-E_v \tau_{sv}} = e^{-E_v \tau_{h'v}}, \tag{2.146}$$

since a halted move is just an unhalted move that encounters an obstacle. Viewing movement backwards in time as propagation from the largest to the smallest imaginary time, the denominator of the first parenthesis of equation (2.141) nicely corresponds to the two occurrences of halted movement that is included in the process in figure 2.9. As earlier stated, we will not uniformly propose random time-shifts and accept them according to the desired probability. Instead, we will propose time-shifts according to the quantile function (also called inverse cumulative distribution function) for the exponential distribution [101]

$$Q(p, E) = -\frac{\ln(1-p)}{E}, \tag{2.147}$$

and accept them with probability 1. Here $p$ is a number between 0 and 1 specifying the fraction of the total probability that should be found between $t = 0$ and $t = Q(p)$. That this method produces the correct result is easy to understand. As explained, for the exponential distribution, 10% of the total probability should be located between $t = 0$ and $t = Q(0.1)$. In the same way, 11% of the total probability should be found below $t = Q(0.11)$. This clearly means that also 1% of the total probability should be found between $t = Q(0.1)$ and $t = (Q = 0.11)$. If we generate random numbers $p$ according to a uniform distribution function, we will then produce values for $p$ that lie between 0.1 and 0.11, 1% of the time and thereby produce values $t = Q(p)$ that that lie between $Q(0.1)$ and $Q(0.11)$ 1% of the time. The same argument goes through for an arbitrarily small interval. We are then clearly generating random values $t$ according to the exponential distribution.

For the case of the time-shift $\tau_{vh}$ in our example, the time shift should therefore be generated as [96]

$$\tau_{vh} = -\frac{\ln(1-u)}{E_t}, \tag{2.148}$$

where $u \in [0, 1)$ is a random number generated from a uniform distribution and the energy in the denominator is the energy in the exponential factor associated with the movement, which in this case is $E_t$. When moving forward in time, this energy is always the energy behind the wormhead in time, while it is the energy ahead of the wormhead in time when moving backwards. If the generated time shift is larger than $\beta$, the modulo of the time shift with respect to $\beta$ should be used. The time shift should be applied in the direction that the wormhead is moving and it should therefore be positive. The energy in the denominator therefore will have to be positive. This can be ensured by performing a rescaling of the energy

$$\begin{aligned} \epsilon_- &= E_- - \min\{E_-, E_+\} + E_{\text{offset}} \\ \epsilon_+ &= E_+ - \min\{E_-, E_+\} + E_{\text{offset}}, \end{aligned} \tag{2.149}$$

where $E_-$ is the energy behind the wormhead in time that is used for propagation forward in time and $E_+$ is the energy ahead of the wormhead in time that is used for propagation backward in time. This rescaling is allowed because it leaves the energy difference $\epsilon_+ - \epsilon_+ = E_+ - E_-$ invariant, and only energy differences are physically relevant [99]. In addition to ensuring positive energies in the denominator, this rescaling can reduce the absolute value of the energies, which leads to a longer average step length for the wormhead movement and potentially a more efficient algorithm. The algorithm is valid for any positive choice of this parameter, but tuning its value can improve performance.

If the shifted time of the wormhead is larger than $\beta$ or smaller than 0, the value will just be shifted to its natural value given by the periodic boundary in the imaginary time direction. If the movement is unhalted, a neighboring site should be chosen with uniform probability, i.e. $1/z$, where $z$ is the number of nearest-neighbors, which, in our case, is $2d$, where $d$ is the dimensionality of the lattice. After the movement, the wormhead should attempt to hop to this neighboring site, and the proposal should be accepted with probability given by the relevant version of equation (2.143). If the proposal is not accepted, the wormhead should turn around.

If the movement is halted, i.e. the generated time shift is larger than the time difference between the wormhead and an upcoming kink, the wormhead should stop right in front of the kink. If the wormhead operator $a^\dagger$ or $a$ is of the same type as the kink operator, the wormhead should just cross the kink and generate a new time-shift without attempting to hop to a neighboring site or turning around. This is a consequence of the commutation relations $[a^\dagger, a^\dagger] = [a, a] = 0$. Similarly, in the case of several components, the wormhead operator will belong to a component and should perform exactly this procedure when encountering a kink corresponding to a different component.

In the case where the wormhead operator is of the conjugate type and same component as the encountered kink operator, the wormhead could either perform a hop to the connected neighboring site, removing the kink pair in the process, hop to a next-neighboring site, shifting the kink pair in space, or turn around. Examples of these actions are shown in figure 2.10. The procedure is as follows. There is an upcoming kink located at site 0. First, the lattice site of the kink that is paired to this upcoming kink is identified (site 1). Then, with probability $1/2d$ for each outcome, a lattice site is chosen between the lattice site of the paired kink itself (1) or one of the neighboring sites to this lattice site (0, 2), excluding the site of the upcoming kink (0). The options are, in other words, site 1 and 2. The probability $1/2d$ is fixed by the probability of proposing a hop to a given neighboring site after an unhalted move, $1/2d$, that we chose earlier, in order for this factor to cancel out in expressions like

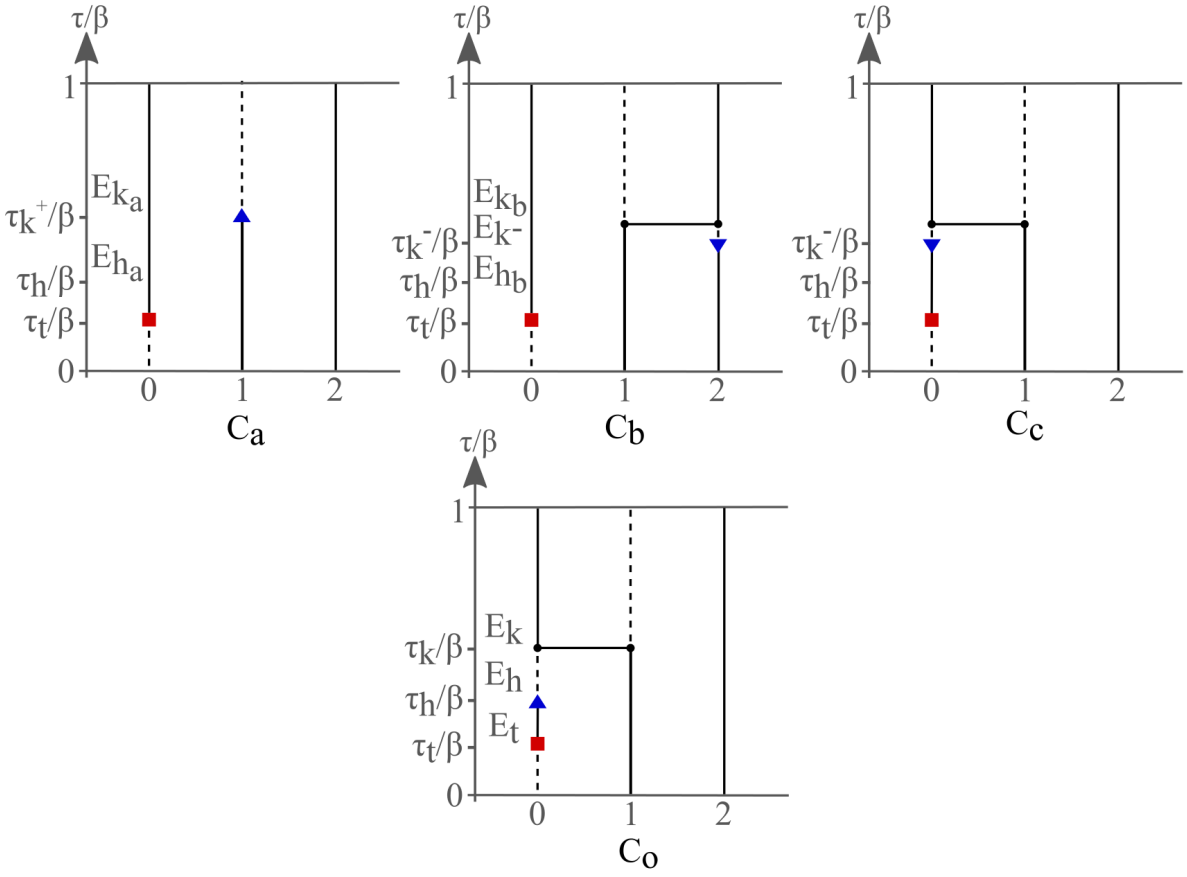


Figure 2.10: Possible moves for a wormhead approaching a kink of conjugate type and same component ($C_o$). The wormhead could delete the kink pair ($C_a$), relink the kink pair ($C_b$) or turn around ($C_c$).

the proposal part of equation (2.141). If the chosen lattice site is the site of the paired kink (1), the wormhead attempts to hop to this site, removing the kink pair in the process. This process is shown in figure 2.10 $C_o \to C_a$. The acceptance probability is once again given by the relevant variant of equation (2.143),

$$\mathcal{P}_A(C_o \to C_a) = \min\left\{1,\ \frac{E_{k_a}\langle\alpha_{k_a}|\, a_1\, |\alpha_{h_a}\rangle}{t\,\langle\alpha_k|\, a_0^\dagger a_1\, |\alpha_h\rangle\,\langle\alpha_h|\, a_0\, |\alpha_t\rangle}\right\} = \min\left\{1,\ \frac{E_{k_a}}{t\,\langle\alpha_t|\, n_0\, |\alpha_t\rangle}\right\}. \tag{2.150}$$

The energy $E_{k_a}$ originates from the reverse process where the unhalted movement takes place backwards in time and where $\alpha_{k_a}$ is the state "behind" the wormhead, i.e. ahead of the wormhead in imaginary time. If the move is not accepted, the wormhead turns around. If, instead, the chosen site is a neighbor to the paired kink (2), the wormhead should attempt to hop to this site, shifting the kink pair, as shown in figure 2.10 $C_o \to C_b$. The acceptance probability is determined in the usual way,

$$\mathcal{P}_A(C_o \to C_b) = \min\left\{1,\ \frac{t\,\langle\alpha_{k_b}|\,a_2^\dagger a_1\,|\alpha_{k^-}\rangle\,\langle\alpha_{k^-}|\,a_2\,|\alpha_{h_b}\rangle}{t\,\langle\alpha_k|\,a_0^\dagger a_1\,|\alpha_h\rangle\,\langle\alpha_h|\,a_0\,|\alpha_t\rangle}\right\} = \min\left\{1,\ \frac{\langle\alpha_{h_b}|\,n_2\,|\alpha_{h_b}\rangle}{\langle\alpha_t|\,n_0\,|\alpha_t\rangle}\right\}. \tag{2.151}$$

and if the move is not accepted, the wormhead should, as usual, turn around. The move where the wormhead performs halted movement to the kink, turns around and returns to its starting point is its own reverse move and therefore clearly also balanced.

If the wormhead is propagating backwards in time, the options when encountering a kink of the opposite type are exactly the same. The options are also the same in the case where the wormhead operator is a creation operator, and the acceptance probabilities are calculated in the same fashion. An example of deletion of a kink pair can, in this case, be seen by interchanging the vertical dotted and solid lines (leaving horizontal lines unchanged) in figure 2.10 $C_o$ and $C_a$, and similarly for the two other possibilities. An example of an insertion of a kink pair is obtained by performing the, earlier described, time-reversal procedure on the process $C_o \to C_a$.

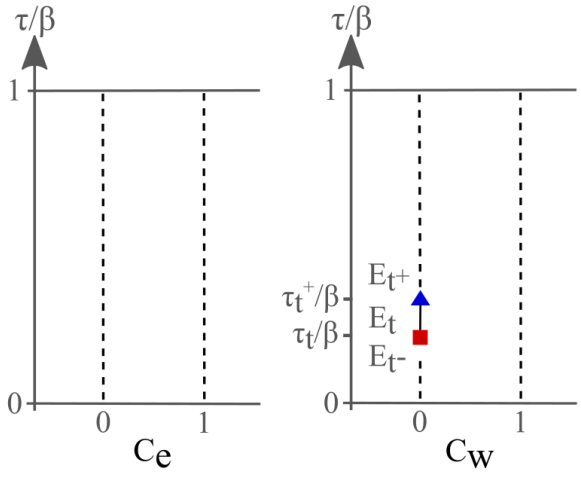


Figure 2.11: The process $C_e \to C_w$ corresponds to the insertion of a worm, and the reverse process corresponds to the deletion of a worm.

All that is left is now to make sure that the insertion and deletion of the worm is also detailed balanced. Examining the configurations $C_e$ and $C_w$ in figure 2.11, and noting that $E_{t+} = E_{t-}$, the fraction between the extended weighting functions can be written as

$$\frac{W(C_w)}{W(C_e)} = \frac{\langle\alpha_t|\,n_0\,|\alpha_t\rangle\,e^{-(\tau_{t+}-\tau_t)(E_t-E_{t-})}}{4\beta s L^d/\mathrm{d}\tau} \longrightarrow \frac{\langle\alpha_t|\,n_0\,|\alpha_t\rangle}{4\beta s L^d/\mathrm{d}\tau}, \tag{2.152}$$

where the factors in the denominator come from the fact that the configuration without a worm is $4\beta s L^d/\mathrm{d}\tau$ degenerate in the extended configuration space. Here a factor 2 comes from the order of the creation and annihilation operator in imaginary time, another factor 2 comes from which operator is assigned to be the head and the tail, $s$ is the number of different components for the operators, $L^d$ is the number of sites that the worm could be placed on and $\beta/\mathrm{d}\tau$ is the number of time intervals where a worm could be inserted. Plugging in equation (2.94), and setting the acceptance probabilities equal to 1, we obtain

$$\frac{\mathcal{P}_P(C_e \to C_w)}{\mathcal{P}_P(C_w \to C_e)} = \frac{\langle \alpha_t | \, n_0 \, | \alpha_t \rangle}{4\beta s L^d / \mathrm{d}\tau}. \tag{2.153}$$

We simply take the nominator on each side equal to 1 over the denominator on the other side. In the process $C_w \to C_e$ this simply corresponds to "randomly" removing one of the $\langle \alpha_1 | \, n_1 \, | \alpha_1 \rangle$ particles, of the correct component, which simply means to reduce the number of particles of that component by one. For the process $C_e \to C_w$ it means that we should randomly generate a component, an operator for the head/tail, a time ordering for the head/tail, a lattice site for the worm and an "infinitesimal" time interval for the worm, according to a uniform distribution function.

**The full procedure for insertion, propagation and deletion can now be summarized as:**

1. Randomly choose a component, an operator for the head/tail, time ordering for the head/tail, a lattice site and an "infinitesimal" time interval
   (a) If the insertion is not possible because the number of particles between the head an tail takes on a a value below 0 or above some maximum set in the model for numerical purposes, potentially perform measurements of relevant observables and return to step 1
   (b) If the insertion is not possible because the time interval is already occupied by a kink, return to step 1
   (c) Otherwise, insert the worm
2. Generate a time-shift according to equation (2.148)
   (a) If the movement is unhalted, randomly choose a neighboring site and attempt to insert a hop to this site
      i. If the hop is accepted according to the relevant version of equation (2.143), perform the hop and move the wormhead an "infinitesimal" time beyond the kink pair before returning to step 2
      ii. If the hop is not possible or not accepted, turn around and return to step 2
   (b) If the movement is halted and the upcoming kink is of the conjugate type and the same component as the wormhead operator, randomly choose a site between the pair-site of the upcoming kink and the nearest-neighbors of the pair-site of the upcoming kink, excluding the original site of the wormhead
      i. If the chosen site is the pair-site of the upcoming kink, attempt to remove the kink pair
         A. If the removal is accepted according to the relevant version of equation (2.150), remove the kink pair, move the wormhead to the pair-site, an "infinitesimal" time beyond the time of the removed kink pair and return to step 2
         B. If the removal is not accepted, turn around and return to step 2
      ii. If the chosen site is a neighbor of the pair-site of the upcoming kink, attempt to shift the kink pair
         A. If the kink pair shift is accepted according to the relevant version of equation (2.151), shift the kink pair, turn the wormhead around, move the wormhead an "infinitesimal" time beyond the time of the shifted kink pair and return to step 2
         B. If the kink pair shift is not accepted or it is not possible to shift the kink pair, return to step 2
   (c) If the movement is halted, but the upcoming kink is of the wrong component or of the same type as the wormhead operator, move the wormhead an "infinitesimal" time beyond the upcoming kink and return to step 2
   (d) If the wormhead reached the wormtail, remove the worm, potentially perform measurements of relevant observables and return to step 1

## 2.7 Comments about the Sign Problem

In section 2.5, we commented on the fact that all the possible values for the normalized weighting function $W(C)/Z$ turned out non-negative and that we therefore could interpret this as a distribution function for the configurations. This is not generally the case, especially not for fermionic systems where the wave function is antisymmetric under exchange of two particles [102]. An exception where the normalized weighting function can be non-negative is e.g. the Hubbard model at half-filling [103]. The negative weighting factors appear in the mapping from a quantum system to classical configurations that one can sum over. The original "weighting operator" $e^{-\beta H}/Z$ is clearly a positive definite operator, but when the trace over this operator is written out as a sum over classical configurations, each term need no longer be positive definite.

It is possible to attempt to avoid the issue of negative weighting factors by splitting the weighting function into its absolute value and phase and instead include the phase factor in the value for the observable that one is averaging over,

$$\langle O \rangle = \frac{\sum_C O[C]\, W[C]}{\sum_C W[C]} = \frac{\frac{1}{Z}\sum_C O[C]\, e^{i\theta[C]}\, \big|W[C]\big|}{\frac{1}{Z}\sum_C e^{i\theta[C]}\, \big|W[C]\big|} = \frac{\big\langle O[C]\, e^{i\theta[C]} \big\rangle_{|W|/Z}}{\big\langle e^{i\theta[C]} \big\rangle_{|W|/Z}}. \tag{2.154}$$

This prescription distorts the notion of sampling typical/important configurations and leads to observables that can potentially oscillate quickly when we move across the configuration space, making it very difficult to obtain reliable results, which is what we call the *sign problem*. The severity of the sign problem is often quantified in terms of the parameter

$$\big\langle e^{i\theta[C]} \big\rangle_{|W|/Z}. \tag{2.155}$$

If this parameter is close to 1, it is still possible to obtain reliable results, but if it approaches 0, our results will be the small reminders of near-cancellation of positive and negative contributions, which typically drown in the noise of the sampling scheme [102]. The same type of problem can arise for bosonic systems in the presence of geometric frustration or spin-orbit coupling. The spin-orbit coupling can e.g. introduce non-component conserving hopping amplitudes that include complex phase factors [60]. A general solution to the sign problem would prove that $P = NP$ [104], i.e. that any computational problem whose solution can be quickly verified (in polynomial time) can also be quickly solved (in polynomial time). A general solution is therefore very hard, if not impossible, to find. The sign problem is however basis dependent (diagonalizing the system would, for instance, solve the problem), and it is possible to find clever solutions for specific systems.

# Chapter 3

# Results

In this chapter we present and discuss the results that were obtained through the Monte Carlo simulations. In the strongly coupled regime, i.e. $t/U \ll 1$, we have performed simulations in both 1 and 2 dimensions (1D/2D) and these results will be presented in parallel. The 1D simulations have generally been performed at lower temperature than the 2D simulations, due to larger thermal fluctuations, in order to obtain the low temperature behavior of the system.

## 3.1 Finite-Size Scaling Analysis

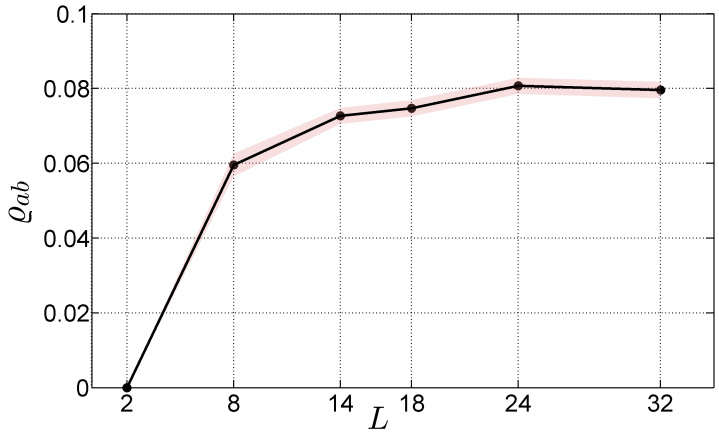


Figure 3.1: 1D: Finite-size scaling analysis performed with $t = 0.2$, $\mu = 0$, $U = 1$, $\lambda = 0.9$ and $\beta = 400$, showing convergence around $L = 24$. Due to symmetric parameters, the curves for the three different drag coefficients were identical, apart from statistical fluctuations. The shaded region displays the estimated error.

To obtain information about real physical systems, one would ideally work with systems consisting of a large number of lattice sites. For computational reasons, one, instead, often attempts to perform simulations with as few lattice sites as possible without introducing substantial finite-size effects. The necessary number of lattice sites that is needed in order to obtain reasonable results for intensive quantities can be determined through a finite-size scaling analysis where the relevant quantities are estimated for different system sizes. If the obtained values converge above a certain system size, this

systems size will be a reasonable choice, at least in the parameter region close to the parameters used in the finite-size scaling analysis.

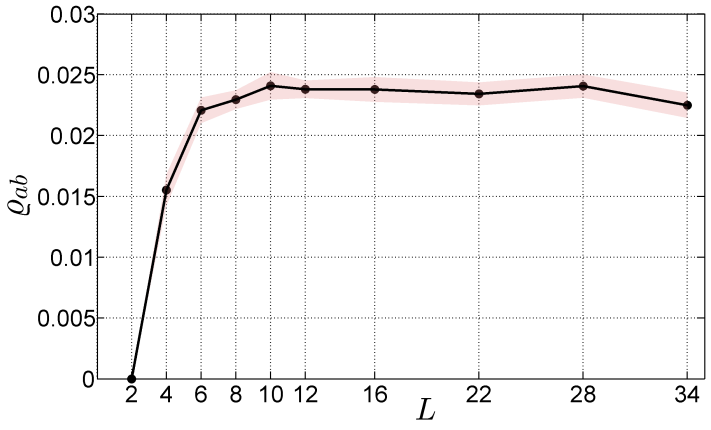


Figure 3.2: 2D: Finite-size scaling analysis performed with $t = 0.1$, $\mu = -0.15$, $U = 1$, $\lambda = 0.9$ and $\beta = 100$, showing convergence around $L = 8$. Due to symmetric parameters, the curves for the three different drag coefficients were identical, apart from statistical fluctuations. The shaded region displays the estimated error.

A solid finite-size scaling analysis should include several samples after the curve looks like it starts to converge to ensure that convergence has actually been achieved. A good example of this can be found in figure 3.2, which shows the finite-size scaling analysis that was performed for the two-dimensional system. A less satisfying example is found in figure 3.1, which shows the 1-dimensional case. Here, it would have been favorable to have data points for even larger system sizes. An even larger system size would, however, have demanded an even larger value for $\beta$ to obtain the low-temperature behavior of the system, which would have been computationally costly. The result of a finite-size scaling analysis with larger $\beta$ would presumably have been that the values for the drag would have converged to a larger value and kept this value for system sizes beyond $L = 32$. The curve would, however, have been expected to converge for about the same system size. Separate investigations did not identify the need for a larger system size than the one obtained from figure 3.1.

## 3.2 Strongly Coupled Regime

In the strongly coupled regime we focus on the area around the first Mott lobe. We are interested in the case where the parameters that contribute to the superfluid drag are completely component-symmetric and, unless stated otherwise, we specialize to this case. The sum of the diagonal superfluid densities $\rho_{\text{sum}} = \rho_{aa} + \rho_{bb} + \rho_{cc}$ as a function of the hopping amplitude and the chemical potential is presented in figure 3.3 and 3.4. The resulting regions where this quantity is zero are similar to the regions without superfluid density in the one-component case. The main exception is the area close to the tip of the Mott lobe, which we will shortly see is a particularly interesting area. Here, the total superfluid density vanishes, but as we see from the figure, we still have diagonal superfluid density.

The total particle number per lattice site, i.e. the filling fraction is presented in figure 3.5 and 3.6. We clearly see that the filling fraction is unity within the first Mott lobe, which is just what we expect.

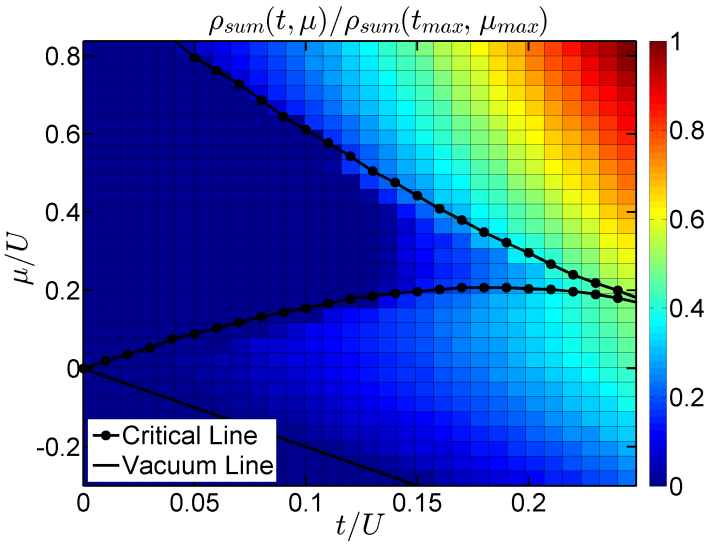


Figure 3.3: 1D: The figure shows the sum over diagonal superfluid densities $\rho_{\text{sum}} = \rho_{aa} + \rho_{bb} + \rho_{cc}$, normalized by the value in the upper right corner, as a function of $t$ and $\mu$ for a system with $U = 1$, $\lambda = 0.9$, $L = 24$, $\beta = 5L/t$ and $m_\alpha = m$. Due to the symmetric parameters, the superfluid density of each component was equal. The critical line and the vacuum line are one-component references. The critical line, separating the Mott-insulating and superfluid phases in the one-component Bose-Hubbard model, is adapted from Fig. 1 in [105]. The vacuum line, marking the region where there are no particles and therefore no superfluid or Mott-insulating phase, is given by $-2t/U$ [35].

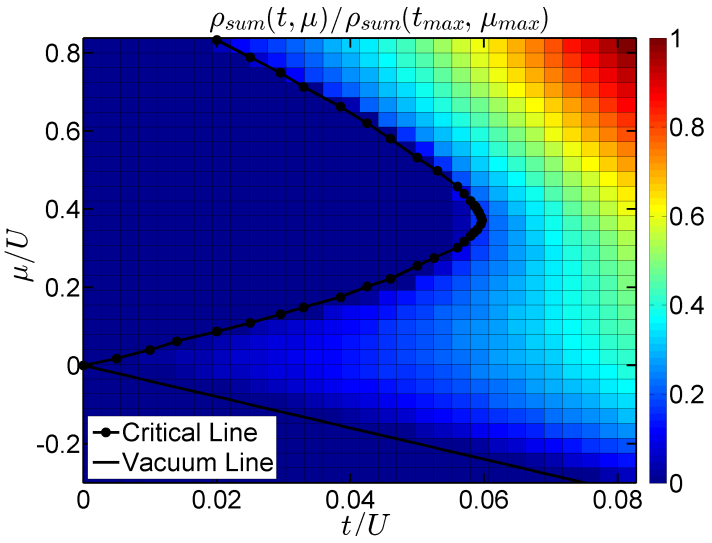


Figure 3.4: 2D: The figure shows sum over diagonal superfluid densities $\rho_{\text{sum}} = \rho_{aa} + \rho_{bb} + \rho_{cc}$, normalized by the value in the upper right corner, as a function of $t$ and $\mu$ for a system with $U = 1$, $\lambda = 0.9$, $L = 10$, $\beta = L/t$ and $m_\alpha = m$. Due to the symmetric parameters, the superfluid density of each component was equal. The one-component critical line is adapted from Fig. 1 in [106], and the vacuum line is given by $-4t/U$ [35].

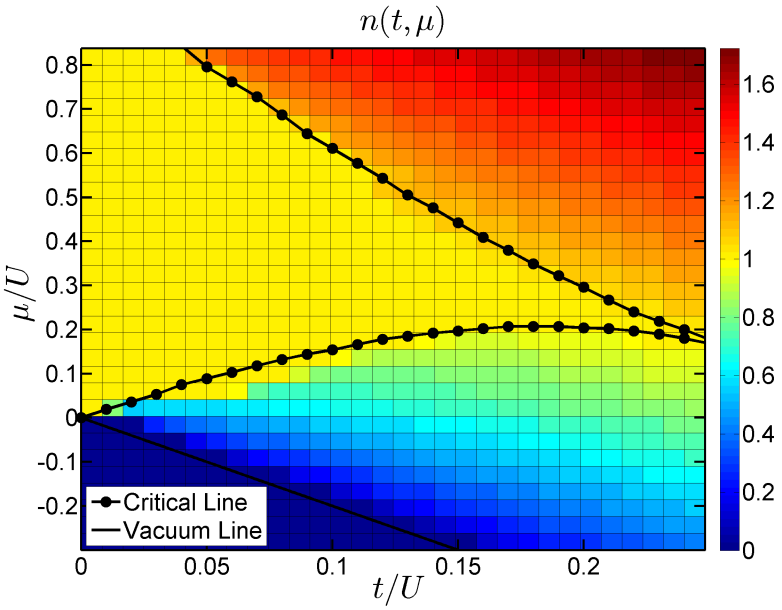


Figure 3.5: 1D: The figure shows the particle density per lattice site, i.e. the filling fraction, as a function of $t$ and $\mu$ for a system with $U = 1$, $\lambda = 0.9$, $L = 24$ and $\beta = 5L/t$. Due to the symmetric parameters, the filling fraction of each component was equal.

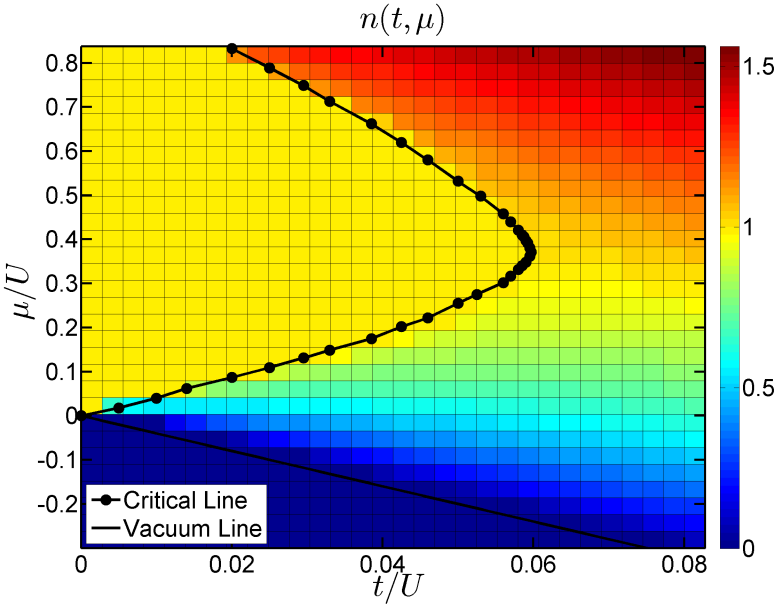


Figure 3.6: 2D: The figure shows the particle density per lattice site, i.e. the filling fraction, as a function of $t$ and $\mu$ for a system with $U = 1$, $\lambda = 0.9$, $L = 10$ and $\beta = L/t$. Due to the symmetric parameters, the filling fraction of each component was equal.

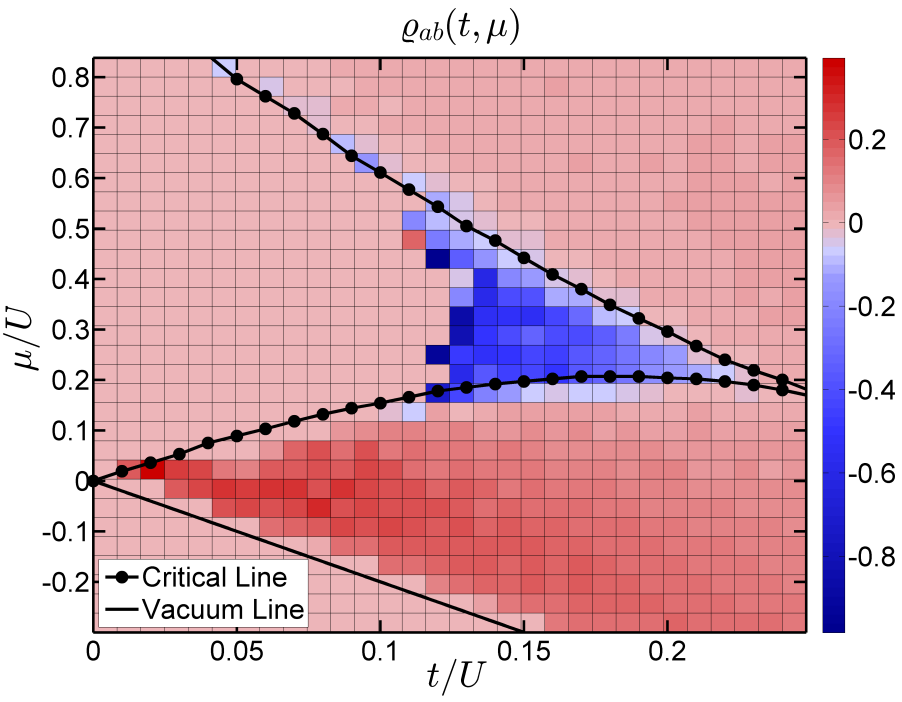


Figure 3.7: 1D: The figure shows the normalized superfluid drag density as a function of $t$ and $\mu$ for a system with $U = 1$, $\lambda = 0.9$, $L = 24$ and $\beta = 5L/t$. Due to the symmetric parameters, the superfluid drag density of each component was equal, apart from statistical fluctuations.

The normalized superfluid drag density, $\varrho_{ab} = \rho_{ab} / \sqrt{\rho_{aa}\rho_{bb}}$, is presented in figure 3.7 and 3.8. Here we find, in both 1 and 2 dimensions, both positive and negative values for the drag. Outside of the one-component Mott-lobe, the drag mostly takes on positive values. The most significant area is located below the Mott lobe, with the largest values obtained for weak hopping amplitude relative to the intracomponent interaction strength. The strong, negative area is located in the, earlier pointed out, region inside the single-component Mott lobe, close to the tip. In the two-dimensional case, we also have a weaker negative area surrounding the single-component Mott lobe. This area is at least much harder to spot, if present at all, in the one-dimensional case. In the two-component case, the superfluid area without a large negative drag (i.e. the region outside of the one-component Mott lobe) is said to belong to a double-superfluid phase [47]. The same area in the three-component case could similarly be classified as a triple-superfluid phase.

Outliers, as well as general deviation from the true value, in the region close to the transition between the supercounterfluid phase and the Mott-insulating phase are caused by increased statistical errors, mainly due to the increased correlation time and the fact that the superfluid densities become very small in this area, meaning that many uncorrelated samples are necessary to resolve the details of the drag statistics. It might also look like there are data points with superfluid drag density without diagonal superfluid density. This is however just because the superfluid density becomes so small that it looks like it vanishes with the scale used in figure 3.3 and 3.4. More precise single-point measurements showed that the region with strong negative drag should extend further back (more in line with the results of [47] in the two-dimensional case), but determining exactly how far was not prioritized.

More precise single-point measurements also revealed that the normalized drag in the negative region

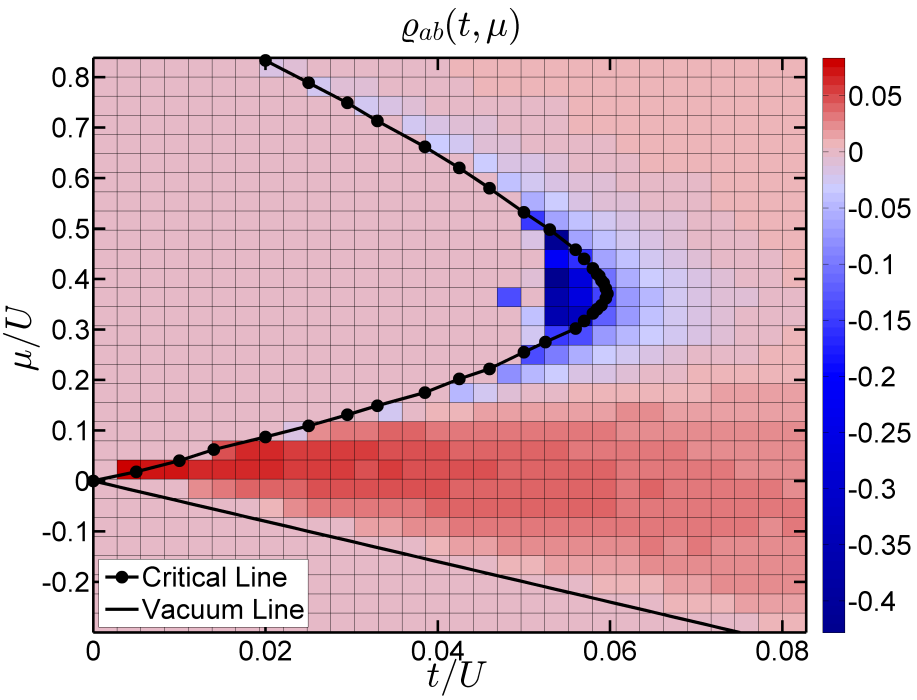


Figure 3.8: 2D: The figure shows the normalized superfluid drag density as a function of $t$ and $\mu$ for a system with $U = 1$, $\lambda = 0.9$, $L = 10$ and $\beta = L/t$. Due to the symmetric parameters, the superfluid drag density of each component was equal, apart from statistical fluctuations.

saturated at $-50\%$, in both one and two dimensions, in contrast to the two-component case where the drag saturated at $-100\%$ [47]. This is due to the fact that it is only possible for the worldlines of two components to wind in opposite directions at the same time. The third component will then either have to not wind at all, or wind in the same direction as one of the two other components. The minimum of $-50\%$ is approached when the contributions are dominated by configurations where only two of the components are winding at the same time (along the same spatial coordinate) and these two are winding the same number of times, in opposite directions. This can easily be checked to produce a normalized drag of $-50\%$ between all components. For asymmetric parameters leading to asymmetric superfluid drag densities, it could be possible to obtain even more negative values for the drag between two of the components.

Returning to the symmetric case, it can also be seen from equation (2.65) that the normalized drags cannot take on values below $-50\%$ in order for the free energy density to be bounded from below. With symmetric parameters, producing symmetric diagonal and off-diagonal superfluid densities, the expression for the free energy takes the form

$$f_s = \frac{1}{2}\rho_{aa}(v_a^2 + v_b^2 + v_c^2) + \rho_{ab}(\vec{v}_a \cdot \vec{v}_b + \vec{v}_a \cdot \vec{v}_c + \vec{v}_b \cdot \vec{v}_c). \tag{3.1}$$

For negative drag, the expression is clearly minimized by taking all superfluid velocities in the same direction. If we take one of the velocities to be much larger than the others, the positive square-term will typically overpower the negative contributions. We therefore also take all the velocities to be equal in magnitude in order to minimize the expression. From the resulting

$$f_s = \frac{3}{2}\rho_{aa}v_a^2 + 3\rho_{ab}v_a^2, \tag{3.2}$$

we then clearly see that the normalized drag $\varrho_{ab}$ cannot go below $-50\%$ in order for the free energy to not be minimized by diverging superfluid velocity. In the two-component case, the lower bound on the normalized drag becomes $-100\%$, which can be easily shown in the same way. This argument can be generalized to the $N$-component case. For $N$ components, equation (3.2) takes the form

$$f_s = \frac{N}{2}\rho_{aa}v_a^2 + \frac{N(N-1)}{2}\rho_{ab}v_a^2, \tag{3.3}$$

where $N(N-1)/2$ is the number of drag terms for a $N$-component system. The lower bound is found by taking $f_s/v_a^2 = 0$, producing

$$\varrho_{\alpha\beta} = -\frac{1}{N-1}. \tag{3.4}$$

Repeating the argument based on the winding of worldlines, one can also easily show that the most negative possible normalized drag one can obtain in the $N$-component case produces the same condition. Assuming the ideal case where each contributing configuration includes, for each spatial coordinate, winding of only two components that wind the same number of times in opposite directions, each spatial coordinate of each configuration will contribute equally to one of the $N(N-1)/2$ drag densities and two of the $N$ diagonal superfluid densities. Each diagonal superfluid density therefore receives $N-1$ times as many contributions as the drag densities, producing the above expression when plugged into the definition of the normalized drag. It is therefore possible that the $N$-component case could feature a negative drag with normalized strength given by equation (3.4).

In the two-component case, the region with normalized drag of $-100\%$ is said to constitute a so-called *supercounterfluid* phase, characterized by $\langle(W_a + W_B)^2\rangle \to 0$ and $\langle(W_a - W_B)^2\rangle \neq 0$ [48]. Similarly, we find $\langle(W_a + W_b + W_c)^2\rangle = 0$ in the case of normalized drag equal to $-50\%$. As we still have non-zero diagonal superfluid density, this is a generalization of the supercounterfluid phase to a three-component system. Since we have symmetric parameters, it follows directly that the total superfluid density vanishes and further that the total superfluid density of each component vanishes. That this is indeed the case follows directly from the definition $\rho_a = \rho_{aa} + 2\rho_{ab}$ and the result for the normalized drag $\rho_{ab} = -\rho_{aa}/2$. Our phase then has vanishing total superfluid density for each component and pairwise counter-directed induced flow between all components, leading to zero net superfluid flow. The $N$-component phase predicted in the previous paragraph would be a straight-forward generalization of this phase.

These phases introduce ordering between pairs of components, but not between all three components. According to [35], such general multicomponent supercounterfluids are best understood in terms a condensate of pairs made up of a particle of one component and a hole of another component, characterized by $\langle\Psi_\beta^\dagger\Psi_\alpha\rangle \neq 0$. Here $\Psi_\alpha$ is the field operator for component $\alpha$, which satisfy $\langle\Psi_\alpha\rangle = 0$ in a supercounterfluid phase. For a 3-component system they predict that one could also have phases with "triple" order displaying co-flow between components $b$ and $c$ and counter-flow between component $a$ and the two other components, characterized by $\langle\Psi_a^\dagger\Psi_b\Psi_c\rangle \neq 0$. Such a phase could be obtained by tuning the chemical potentials and the interaction strengths to divide the lattice sites evenly between an occupation number state with one particle of type $a$ and an occupation number state with one particle of both type $b$ and $c$.

In the two-component case, the effect of attractive intercomponent interactions has been investigated, leading to positive drag due to particles of different types being attracted to each other and therefore having a tendency of moving together in the same direction [47]. For strong attractive intercomponent interactions, a saturated normalized drag of 100% has been obtained, a so-called *paired superfluid* phase [36, 47]. The two-directional issue for three-component systems does not affect co-flow and normalized drags of 100% would not make the free energy in equation (2.65) unbounded from below. The last point can be shown in the same way as for the negative case, but this time with the superfluid velocities as oppositely directed as possible. It could therefore be possible to obtain a similar phase in the three-component case.

In the two-component case, the connection between the model parameters and the resulting drag can be understood in terms of two-body collisions in the momentum space formulation of the problem [107]. In the case of filling factor below 1, it will then be possible for a particle of e.g. component $a$ to approach a particle of component $b$ from the left, transferring momentum to send the particle of type $b$ over to an empty lattice site on the right. These sorts of processes generate co-flow of components, producing a positive drag. For larger filling factor, it would be less favorable for the particle of type $b$ to hop to the right, as this site would most likely already be occupied by at least one particle. A positive region below the Mott lobe makes sense when viewed in this light. In the case of a filling factor close to 1, a particle of type $a$ approaching a particle of type $b$ from the left will leave a rare unoccupied site behind, making it very favorable for the particle of type $b$ to hop in the opposite direction to avoid paying the intercomponent interaction energy. This type of back-flow, familiar from Mott-insulating physics [35, 108, 109], can produce a negative superfluid drag. These intuitive pictures are also clearly able to qualitatively describe the results that we have presented for the three-component case so far.

## 3.3 Weakly Coupled Regime

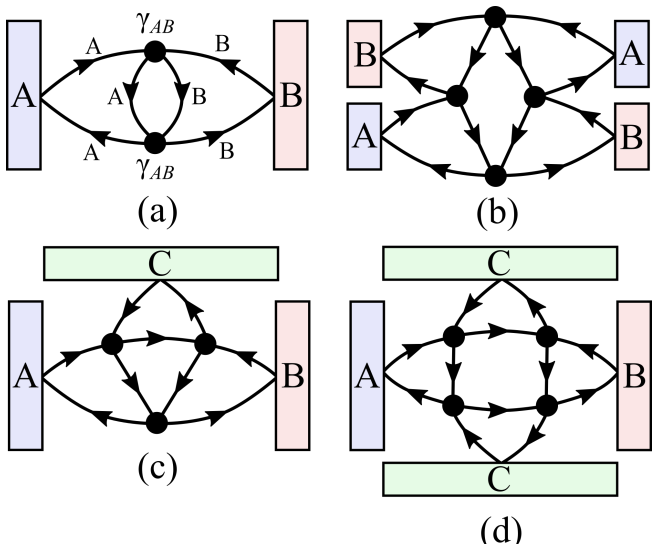


Figure 3.9: Feynman diagrams illustrating terms in the mean-field perturbation series of the drag expanded in terms of the intercomponent interaction strengths. (a) corresponds to a second-order term, (b) and (d) to fourth-order terms and (c) to a third-order term. The condensates of the different components are represented as rectangular blocks, and the lines represent excitations that move in and out of the condensates and interact with each other. Each vertex introduces a factor $\lambda_{\alpha\beta}$, which is denoted as $\gamma_{\alpha\beta}$ in the diagrams. The figure was created by Stian Hartman.

We now turn our attention to the weak-coupling regime and investigate how the the introduction of component $c$ affects the drag between components $a$ and $b$, motivated by mean-field calculations performed by Stian Hartman [107]. As shown in the previously mentioned paper [1], in contrast to the two-component case where the drag $\rho_{ab}$ is independent of the sign of the intercomponent interaction strength $\lambda_{ab}$, the drag $\rho_{ab}$ will, in the three-component case, generally depend on the sign of all three intercomponent interactions strengths. This conclusion was obtained using both numerical diagonalization and a perturbative approach at the mean-field level as well as the quantum Monte Carlo results that will be presented in this section. In the perturbative approach, the drag was expanded to fourth order in the intercomponent interaction strengths, producing

$$\rho_{ab} = \rho_{ab}^{(2)} + \rho_{ab}^{(3)} + \rho_{ab}^{(4)}, \tag{3.5}$$

with

$$\begin{aligned} \rho_{ab}^{(2)} &\propto \quad \lambda_{ab}^2 \\ \rho_{ab}^{(3)} &\propto -\lambda_{ab}\lambda_{ac}\lambda_{bc} \\ \rho_{ab}^{(4)} &\propto \quad \lambda_{ab}^2\lambda_{ab}^2, \quad \lambda_{ab}^2\lambda_{ac}^2, \quad \lambda_{ab}^2\lambda_{bc}^2, \quad \lambda_{ac}^2\lambda_{bc}^2. \end{aligned} \tag{3.6}$$

Here, the second-order terms correspond to collision processes with direct interaction between component $a$ and $b$. The fourth-order terms correspond to processes where there is only interaction between component $a$ and $b$, processes where the interaction between component $a$ and $b$ is completely mediated by component $c$, and processes where component $a$ interacts directly with both the two other

components. The third-order terms, which are the only ones giving contributions that depend on the sign of the intercomponent interaction strengths, correspond to the simplest possible processes involving direct interaction between all three components. Terms of even higher order are expected to be less influential.

The above discussed perturbation terms can be illustrated in terms of Feynman diagrams where excitations of the condensates of the different components interact with each other. Figure 3.9 (a) and (b) show processes corresponding to second-order and fourth-order terms where there is only direct interaction between component $a$ and $b$. These are the only types of processes that take place in two-component systems. The diagram in (d) represents a fourth-order process where the interaction between component $a$ and $b$ is completely mediated by component $c$, while the diagram in (c) represents a third-order process where all three components interact directly. The higher-order processes can be interpreted as effective interaction processes between component $a$ and $b$ with renormalized interaction strengths. Examples of this is presented in figure 3.10, providing us with the picture of the higher-order contributions as effective two-body interactions with more complex interaction mechanisms due to the presence of additional particles.

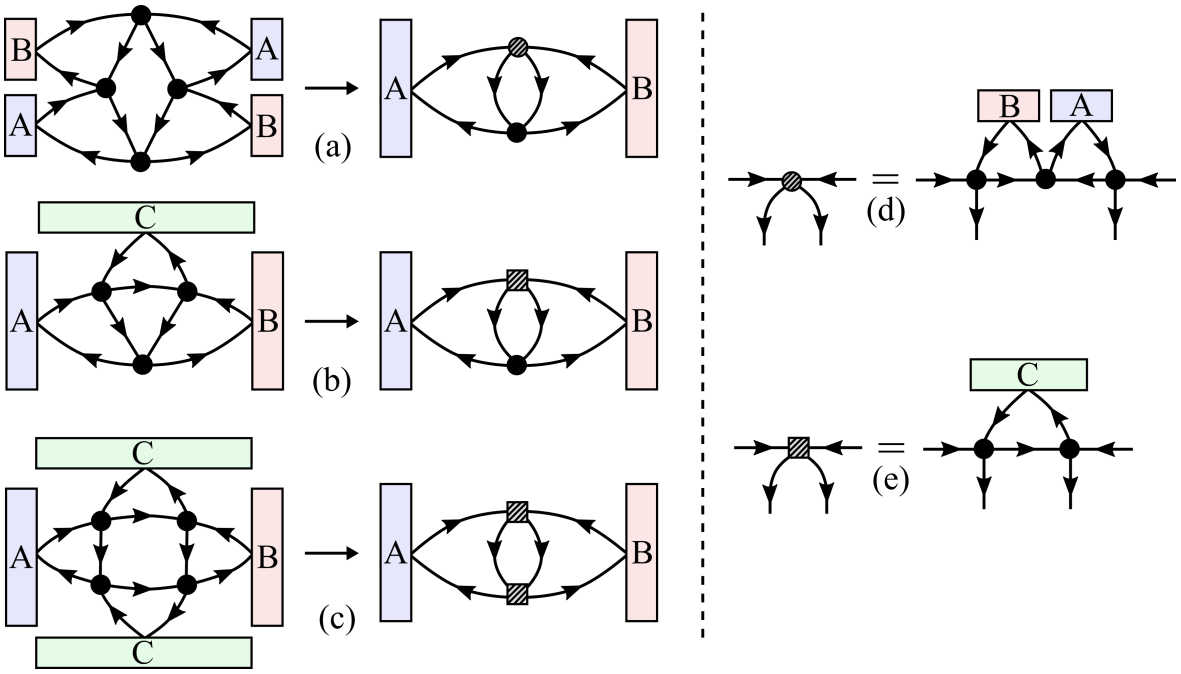


Figure 3.10: Higher-order processes redrawn as two-component processes with renormalized interactions. The renormalized vertex in (e) introduces the effect of a third component on the interaction between component $a$ and $b$. The second-order process in (a) consists of an even number of $\lambda_{ab}$-vertices, producing a positive sign. Similarly the the fourth-order process in (c) consists of an even number of the renormalized vortex displayed in (e), producing an overall positive sign. The third-order process in (b), on the other hand, includes both a $\lambda_{ab}$-vertex and a renormalized vertex including the effect of component $c$, producing an overall negative sign. The figure was created by Stian Hartman.

In figure 3.11, we present the effect that the intercomponent interaction strength $\lambda_{ac}$ and $\lambda_{bc}$ has on the drag between the superfluid components $a$ and $b$, using both quantum Monte Carlo simulations and numerical diagonalization of the mean-field Hamiltonian. From the point of view of the

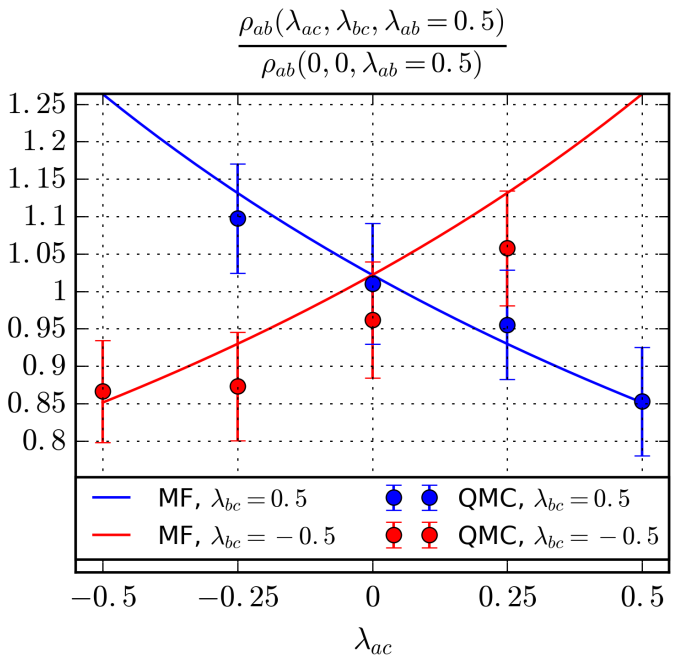


Figure 3.11: 2D: Comparison between results from mean-field theory obtained by Stian Hartman and quantum Monte Carlo simulations for a system with $t = 1$, $n_\alpha = n = 0.3$ $U = 1$, $L = 10$ and $\beta = 10$. The error bars include the error in both the nominator and the denominator.

perturbation series, for the parameter region displayed in the figure, the dominating corrections to the second-order contributions are the third-order contributions. The second-order contributions are constant for constant $\lambda_{ab}$, and the drag therefore either increases or decreases with increasing $\lambda_{ac}$, depending on the sign of $\lambda_{bc}$, in accordance with the expression for the third-order contributions. For smaller or vanishing $\lambda_{ab}$, fourth-order terms where the interaction between $a$ and $b$ is completely mediated by $c$ start to dominate, producing curves that approach symmetric, parabolic shapes that increase monotonically with the absolute value of $\lambda_{ac}$.

The numerical values for the drag that were obtained through quantum Monte Carlo were about 40% larger than the mean-field values, but the relative values displayed in the figure corresponded well. Overall, the Monte Carlo simulations clearly support the qualitative behavior of drag that was obtained from mean-field theory. Simulations with fixed particle number were performed by tuning the chemical potential in order to produce the desired average particle numbers. The values for the chemical potentials were found by starting from values provided by mean-field theory and performing iterative simulations until a sufficient accuracy had been achieved. The rest of the details of the numerics can be found in the appendix.

# Chapter 4

# Conclusion

We have investigated the superfluid drag density in the superfluid phase of a three-component Bose-Hubbard model by means of path integral Monte Carlo simulations in both one and two dimensions. As a function of the hopping amplitude and chemical potential, for the case of component-symmetric parameters, the drag was found to take on positive values away from the one-component Mott-lobe, and negative values around the tip of the one-component Mott-lobe. On the inside of the lobe, we found a supercounterfluid phase with zero total superfluid density. This phase involved a normalized drag of $-50\%$ between all components, in contrast to the two-component case where the normalized drag saturated at $-100\%$ [47]. This was an expected result due to the nature of winding of three different components in two opposite directions, as well as the condition that the free energy should be bounded from below. Based on these results we propose that it is possible that a general $N$-component superfluid system could harbor a supercounterfluid phase with normalized drag equal to -1/(N-1).

In the weakly coupled limit we examined the effect of the introduction of a third component on the drag between component $a$ and $b$. In accordance with mean-field results obtained by Stian Hartman [107], the drag between component $a$ and $b$ was found to depend non-trivially on the details of all three intercomponent interaction strengths. In this thesis we presented Monte Carlo results supporting the mean-field behavior in the parameter region where the drag between component $a$ and $b$, as a function of the interaction between $a$ and $c$, was found to be dominated by third-order terms from the point of view of a mean-field perturbation series where the drag is expanded in terms of intercomponent interaction strengths. Such third-order terms could be be attributed to the simplest possible collision processes involving direct interaction between all three components. In this parameter region, we found an approximately linear dependence on the interaction strength between component $a$ and $c$, where the slope was determined by the interaction between $b$ and $c$ for fixed interaction between $a$ and $b$. This behavior is in stark contrast to the two-component case, where the drag is independent of the sign of the intercomponent interaction strength. Further details about the mean-field results can be found in [1].

This thesis provides a basis for further research concerning the superfluid drag in three-component systems. Future work could e.g. include the search for the proposed generalization of a paired superfluid phase in the case of attractive intercomponent interactions or other composite co-/counter-directed phases with triple order. The dependence of the superfluid drag on the details of the intercomponent interaction strengths could also be explored in the strongly coupled regime, in e.g. the triple-superfluid region or the supercounterfluid region. The quantum Monte Carlo methods applied in this thesis, as well as the mean-field methods from [1], are easily generalized to more than three components, opening up for the investigation of even more complicated behavior.

# Bibliography


[1] S. Hartman, E. Erlandsen, and A. Sudbø, ArXiv e-prints (2018), arXiv:1805.11156.

[2] The ALPS Project, http://alps.comp-phys.org/.

[3] B. Bauer et al., J. Stat. Mech. P05001 (2011).

[4] A.F. Albuquerque et al., J. of Magn. and Magn. Materials **310**, 1187 (2007).

[5] M. H. Anderson, J. R. Ensher, M. R. Matthews, C. E. Wieman, and E. A. Cornell, Science **269**, 198 (1995).

[6] K. B. Davis, M. -O. Mewes, M. R. Andrews, N. J. van Druten, D. S. Durfee, D. M. Kurn, and W. Ketterle, Phys. Rev. Lett. **75**, 3969 (1995).

[7] E. A. Cornell and C. E. Wieman, Rev. Mod. Phys. **74**, 875 (2002).

[8] W. Ketterle, Rev. Mod. Phys. **74**, 1131 (2002).

[9] E. H. Lieb, J. P. Solovej, R. Seiringer, and J. Yngvason, *The Mathematics of the Bose Gas and its Condensation* (Birkhäuser, 2005).

[10] I. Bloch, Nature Physics **1**, 23 (2005).

[11] C. J. Pethick and H. Smith, *Bose-Einstein Condensation in Dilute Gases*, 2nd ed. (Cambridge University Press, 2008).

[12] I. Bloch, J. Dalibard, and S. Nascimbène, Nature Physics **8**, 267 (2012).

[13] D. M. Stamper-Kurn and M. Ueda, Rev. Mod. Phys. **85**, 1191 (2013).

[14] Y.-J. Lin, K. Jiménez-García, and I. B. Spielman, Nature **471**, 83 (2011).

[15] V. Galitski and I. B. Spielman, Nature **494**, 49 (2013).

[16] M. Lewenstein, A. Sanpera, and V. Ahufinger, *Ultracold Atoms in Optical Lattices: Simulating quantum many-body systems* (Oxford University Press, 2012).

[17] C. J. Myatt, E. A. Burt, R. W. Ghrist, E. A. Cornell, and C. E. Wieman, Phys. Rev. Lett. **78**, 586 (1997).

[18] D. M. Harber, H. J. Lewandowski, J. M. McGuirk, and E. A. Cornell, Phys. Rev. A **66**, 053616 (2002).

[19] G. Kleine Büning, J. Will, W. Ertmer, E. Rasel, J. Arlt, C. Klempt, F. Ramirez-Martinez, F. Piéchon, and P. Rosenbusch, Phys. Rev. Lett. **106**, 240801 (2011).

[20] G. Modugno, M. Modugno, F. Riboli, G. Roati, and M. Inguscio, Phys. Rev. Lett. **89**, 190404 (2002).

[21] G. Thalhammer, G. Barontini, L. De Sarlo, J. Catani, F. Minardi, and M. Inguscio, Phys. Rev. Lett. **100**, 210402 (2008).

[22] S. B. Papp, J. M. Pino, and C. E. Wieman, ArXiv e-prints (2008), arXiv:0802.2591.

[23] D. M. Stamper-Kurn, M. R. Andrews, A. P. Chikkatur, S. Inouye, H.-J. Miesner, J. Stenger, and W. Ketterle, Phys. Rev. Lett. **80**, 2027 (1998).

[24] M. D. Barrett, J. A. Sauer, and M. S. Chapman, Phys. Rev. Lett. **87**, 010404 (2001).

[25] T. Kuwamoto, K. Araki, T. Eno, and T. Hirano, Phys. Rev. A **69**, 063604 (2004).

[26] H. Schmaljohann, M. Erhard, J. Kronjäger, M. Kottke, S. van Staa, L. Cacciapuoti, J. J. Arlt, K. Bongs, and K. Sengstock, Phys. Rev. Lett. **92**, 040402 (2004).

[27] J. Catani, L. De Sarlo, G. Barontini, F. Minardi, and M. Inguscio, Phys. Rev. A **77**, 011603 (2008).

[28] Artur Widera, Fabrice Gerbier, Simon Fölling, Tatjana Gericke, Olaf Mandel, and Immanuel Bloch, Phys. Rev. Lett. **95**, 190405 (2005).

[29] S. Trotzky, P. Cheinet, S. Fölling, M. Feld, U. Schnorrberger, A. M. Rey, A. Polkovnikov, E. A. Demler, M. D. Lukin and I. Bloch, Science **319**, 295 (2008).

[30] Artur Widera, Stefan Trotzky, Patrick Cheinet, Simon Fölling, Fabrice Gerbier, Immanuel Bloch, Vladimir Gritsev, Mikhail D. Lukin, and Eugene Demler, Phys. Rev. Lett. **100**, 140401 (2008).

[31] David M. Weld, Patrick Medley, Hirokazu Miyake, David Hucul, David E. Pritchard, and Wolfgang Ketterle, Phys. Rev. Lett. **103**, 245301 (2009).

[32] Bryce Gadway, Daniel Pertot, René Reimann, and Dominik Schneble, Phys. Rev. Lett. **105**, 045303 (2010).

[33] A. F. Andreev and E. P. Bashkin, Soviet Physics JETP **42**, 164 (1975).

[34] J. Nespolo, G. E. Astrakharchik, and A. Recati, New J. Phys. 19, 125005 (2017).

[35] V. Svistunov, E. S. Babaev, N. V. Prokof'ev, *Superfluid States of Matter* (CRC Press, 2015).

[36] A. Kuklov, N. Prokof'ev, and B. Svistunov, Phys. Rev. Lett. **92**, 030403 (2004).

[37] Z. Qi-Zhong and W. Biao, Chin. Phys. B **24** 050507 (2015).

[38] M. A. Alpar, S. A. Langer, and J. A. Sauls, Astrophys. J. **282**, 533 (1984).

[39] E. Babaev, Phys. Rev. D **70**, 043001 (2004).

[40] J. Garaud, K. A. H. Sellin, J. Jäykkä, and E. Babaev, Phys. Rev. B **89**, 104508 (2014).

[41] L. Onsager, Il Nuovo Cimento **6**, 2 Supplement (1949).

[42] R. P. Feynman, *Progress in Low Temperature Physics: Chapter II Application of Quantum Mechanics to Liquid Helium* (Elsevier, 1955).

[43] E. K. Dahl, E. Babaev, S. Kragset, and A. Sudbø, Phys. Rev. B **77**, 144519 (2008).

[44] E. K. Dahl, E. Babaev, and A. Sudbø, Phys. Rev. B **78**, 144510 (2008).

[45] E. K. Dahl, E. Babaev, and A. Sudbø, Phys. Rev. Lett. **101**, 255301 (2008).

[46] V. M. Kaurov, A. B. Kuklov, and A. E. Meyerovich, Phys. Rev. Lett. **95**, 090403 (2005).

[47] K. Sellin and E. Babaev, Phys. Rev. B **97**, 094517 (2018).

[48] F. Lingua, M. Guglielmino, V. Penna, and B. C. Sansone, Phys. Rev. A **92**, 053610 (2015).

[49] D. V. Fil and S. I. Shevchenko, Phys. Rev. A **72**, 013616 (2005).

[50] Y. Yanay and E. J. Mueller, ArXiv e-prints (2012), arXiv:1209.2446.

[51] J. Linder and A. Sudbø, Phys. Rev. A **79**, 063610 (2009).

[52] Patrick P. Hofer, C. Bruder, and Vladimir M. Stojanović, Phys. Rev. A **86**, 033627 (2012).

[53] A. Posazhennikova, Rev. Mod. Phys. **78**, 1111 (2006).

[54] N. N. Bogoliubov, J. Phys. (USSR) **11**, 23 (1947).

[55] C. Becker, P. Soltan-Panahi, J. Kronjäger, S. Dörscher, K. Bongs, and K. Sengstock, New Journal of Physics, **12**, 065025 (2010).

[56] G.-B. Jo, J. Guzman, C. K. Thomas, P. Hosur, A. Vishwanath, and D. M. Stamper-Kurn, Phys. Rev. Lett. **108**, 045305 (2012).

[57] C. Chin, R. Grimm, P. Julienne, and E. Tiesinga, Rev. Mod. Phys. **82**, 1225 (2010).

[58] H. K. Andersen, *Bose-Einstein condensates in optical lattices*, PhD thesis, University of Aarhus (2008).

[59] G.-H. Chen and Y.-S. Wu, Phys. Rev. A **67**, 013606 (2003).

[60] E. Thingstad, *Two-Component Spin-Orbit Coupled Ultracold Atoms in the Weak and Strong Coupling Regimes*, Master's thesis, NTNU (2017).

[61] N. Marzari, A. A. Mostofi, J. R. Yates, I. Souza, and D. Vanderbilt, Rev. Mod. Phys. **84**, 1419 (2012).

[62] M. Greiner, O. Mandel, T. Esslinger, T. W. Hänsch, and I. Bloch, Nature **415**, 39 (2002).

[63] J. K. Freericks and H. Monien, EPL **26**, 545 (1994).

[64] J. F. Allen and H. Jones, Nature **141**, 243 (1938).

[65] A. Schmitt, ArXiv e-prints (2014), arXiv:1404.1284.

[66] P. Kapitza, Nature **141**, 74 (1938).

[67] J. F. Allen and A. D. Misener, Nature **141**, 75 (1938).

[68] W. H. Keesom and A. P. Keesom, Physica **2**, 557 (1935).

[69] L. Landau, Phys. Rev. **60**, 356 (1941).

[70] D. J. Bishop and J. D. Reppy, Phys. Rev. Lett. **40**, 1727 (1978).

[71] The Royal Swedish Academy of Sciences, *Topological phase transitions and topological phases of matter* (2016), Scientific Background on the Nobel Prize in Physics 2016.

[72] L. Tisza, Nature **141**, 913 (1938).

[73] I. Carusotto and Y. Castin, Comptes Rendus Physique **5**, 107 (2004).

[74] A. Einstein, Ber. Berl. Akad. 261 (1924); ibid. 3 (1925).

[75] P. B. Weichman, Phys. Rev. B **38**, 8739 (1988).

[76] S. Weinzierl, ArXiv e-prints (2000), arXiv:hep-ph/0006269.

[77] W. H. Press, S. A. Teukolsky, W. T. Vetterling, and B. P. Flannery, *Numerical Recipes in C++. The Art of Scientific Computing*, Second ed. (Cambridge University Press, 2002).

[78] S. Jain, *Monte Carlo Simulations Of Disordered Systems* (World Scientific, 1992).

[79] J. O. Andersen, *Introduction to Statistical Mechanics*, First ed. (Akademika forlag, 2012).

[80] W.-K. Ching, X. Huang, M. K. Ng, and T.-K. Siu, *Markov Chains - Models, Algorithms and Applications*, 2nd ed. (Springer, 2013).

[81] R. G. Gallager, *Discrete Stochastic Processes* (Springer, 1996).

[82] V. I. Manousiouthakis and M. W. Deem, J. Chem. Phys. **110**, 2753 (1999).

[83] N. Metropolis, A. W. Rosenbluth, M. N. Rosenbluth, and A. H. Teller, J. Chem. Phys. **21**, 1087 (1953).

[84] E. V. Herland, *Theoretical studies of twocomponent superfluids and superconductors*, Ph.D. thesis, NTNU (2012).

[85] M. E. J. Newman and G. T. Barkema, *Monte Carlo Methods in Statistical Physics* (Oxford University Press, 1999).

[86] R. H. Swendsen and J.-S. Wang, Phys. Rev. Lett. **58**, 86 (1987).

[87] U. Wolff, Phys. Rev. Lett. **62**, 361 (1989).

[88] H. Müller-Krumbhaar and K. Binder, J. of Stat. Phys. 8: 1. (1973).

[89] B. Efron and R. Tibshirani, Statistical Science, **1**, 1 (1986).

[90] M. Matsumoto and T. Nishimura, ACM Trans. Model. Comput. Simul. **8**, 3 (1998).

[91] A. Wipf, *Statistical Approach to Quantum Field Theory* (Springer, 2013).

[92] J. J. Sakurai and S. F. Tuan, *Modern Quantum Mechanics* (Addison-Wesley, 1994).

[93] E. L. Pollock and D. M. Ceperley, Phys. Rev. B **36**, 8343 (1987).

[94] N. V. Prokof'ev and B. V. Svistunov, Phys. Rev. B **61**, 11282 (2000).

[95] K. Jiménez-García, L. J. LeBlanc, R. A. Williams, M. C. Beeler, A. R. Perry, and I. B. Spielman, Phys. Rev. Lett. 108, 225303 (2012).

[96] P. N. Ma, *Numerical Simulations of Bosons and Fermions in Three Dimensional Optical Lattices*, Ph.D. thesis, ETH Zürich (2013).

[97] N. V. Prokof'ev, B. V. Svistunov, and I. S. Tupitsyn, Journal of Experimental and Theoretical Physics **87**, 310 (1998).

[98] N. V. Prokof'ev, B. V. Svistunov, and I. S. Tupitsyn, Journal of Experimental and Theoretical Physics **87** , 310 (1998).

[99] L. Pollet, K. V. Houcke, and S. M. A. Rombouts, Journal of Computational Physics **225/2**, 2249-2266 (2007).

[100] C. Trefzger, C. Menotti, B. Capogrosso-Sansone, and M. Lewenstein, J. Phys. B: At. Mol. Opt. Phys. **44**, 193001 (2011).

[101] NIST/SEMATECH, *e-Handbook of Statistical Methods*.

[102] E. Y. Loh, Jr., J. E. Gubernatis, R. T. Scalettar, S. R. White, D. J. Scalapino, and R. L. Sugar, Phys. Rev. B **41**, 9301 (1990).

[103] J. E. Hirsch, Phys. Rev. B **31**, 4403 (1985).

[104] M. Troyer and U.-J. Wiese, Phys. Rev. Lett. **94**, 170201 (2005).

[105] S. Ejima, H. Fehske, F. Gebhard, K. zu Münster, M. Knap, E. Arrigoni, and W. von der Linden, Phys. Rev. A **85**, 053644 (2012).

[106] B. Capogrosso-Sansone, Ş. G. Söyler, N. Prokof'ev, and B. Svistunov, Phys. Rev. A **77**, 015602 (2008).

[107] S. Hartman, *Drag and Phases of Interacting and Spin–Orbit Coupled Superfluid Bose–Einstein Condensates*, Master's thesis, NTNU (2018).

[108] A. B. Kuklov and B. V. Svistunov, Phys. Rev. Lett. **90**, 100401 (2003).

[109] E. Altman, W. Hofstetter, E. Demler, and M. D. Lukin, New Journal of Physics **5**, 113 (2003).

[110] R. H. Swendsen and J.-S. Wang, Phys. Rev. Lett. **57**, 2607 (1986).

[111] D. J. Earl and M. W. Deem, Phys. Chem. Chem. Phys. **7**, 3910 (2005).

[112] T. Ohgoe and N. Kawashima, Phys. Rev. A **83**, 023622 (2011).

# Appendix A

# Details of the Numerics

In the simulations producing results presented in this thesis, we started with an empty configuration and performed typically $10^6 - 10^8$ worm insertions in order to thermalize the system. After the initial thermalization insertions, we collected $10^6 - 10^8$ samples with $10^1 - 10^5$ worm insertions between each sample. In the weakly coupled regime, it was not necessary to perform a large number of worm insertions between each sample in order to generate independent configurations. On the other hand, the drag density was very small in this regime, meaning that a large number of samples was needed in order to resolve the details of the winding number statistics. For the weak-coupling simulations $10^8 - 10^9$ samples were collected with $10^1 - 10^2$ worm insertions between each sample. In the strongly coupled regime, more worm insertions were needed between each sample. At the same time, the drag density was, generally, significantly larger than in the weakly coupled regime. The results in the strongly coupled region were therefore obtained from $10^6$ samples with $10^3 - 10^5$ worm insertions between each sample. High-precision single-point measurements in the supercounterfluid region were obtained using as many as $10^6$ worm insertions between each sample. Further investigation of this region could potentially benefit from the use of parallel tempering [84, 110, 111] in order to combat the large correlation time. It could also be possible to apply a generalization of the pair-worm algorithm in [112], which has shown increased efficiency in the supercounterfluid phase of a two-component system.

Throughout the thesis, error estimates have been obtained through bootstrapping. The offset parameter used in the rescaling of the on-site energy, $E_{\text{offset}}$ in equation (2.149), was typically set between 0.1 and 0.01. The normalization data point in figure 3.11 was obtained using $\mu_A = -3.6053$, $\mu_B = -3.6068$, $\mu_C = -3.7468$ producing $n_A = 0.301$, $n_B = 0.297$ and $n_C = 0.300$. The rest of the chemical potentials used in this figure are displayed in table A.1 and A.2. The mean-field values that were used as starting points in order to tune the chemical potentials were obtained from the expression [107]

$$\mu_\alpha = -4t + U\big(n_\alpha + \lambda_{\alpha\beta} n_\beta + \lambda_{\alpha\gamma} n_\gamma\big), \tag{A.1}$$

where $\alpha$, $\beta$ and $\gamma$ all represent different components, i.e $\alpha \neq \beta \neq \gamma$.

The code provided by Even Thingstad that was mentioned in the preface concerned the case of a two-component system in one spatial dimension. In the work related to this thesis, the code was refined, generalized to three components in both one and two dimensions and prepared for large-scale supercomputer simulations.

| $\lambda_{AC}$ | $\mu_A$ | $\mu_B$ | $\mu_C$ | $n_A$ | $n_B$ | $n_C$ |
|---|---|---|---|---|---|---|
| -0.25 | -3.6797 | -3.4594 | -3.6797 | 0.303 | 0.301 | 0.303 |
| 0 | -3.6024 | -3.4595 | -3.6021 | 0.301 | 0.302 | 0.302 |
| 0.25 | -3.5303 | -3.4609 | -3.5294 | 0.300 | 0.300 | 0.301 |
| 0.5 | -3.4591 | -3.4596 | -3.4590 | 0.301 | 0.300 | 0.302 |

Table A.1: Values for the chemical potentials and the resulting particle densities for each of the data points in figure 3.11 with $\lambda_{bc} = 0.5$.

| $\lambda_{AC}$ | $\mu_A$ | $\mu_B$ | $\mu_C$ | $n_A$ | $n_B$ | $n_C$ |
|---|---|---|---|---|---|---|
| -0.5 | -3.7609 | -3.7604 | -4.0638 | 0.299 | 0.300 | 0.298 |
| -0.25 | -3.6802 | -3.7621 | -3.9811 | 0.301 | 0.300 | 0.300 |
| 0 | -3.6018 | -3.7599 | -3.9068 | 0.302 | 0.301 | 0.299 |
| 0.25 | -3.5301 | -3.7593 | -3 8348. | 0.300 | 0.304 | 0.300 |

Table A.2: Values for the chemical potentials and the resulting particle densities for each of the data points in figure 3.11 with $\lambda_{bc} = -0.5$.